Spiropyran-based materials and MOF crystal imaging

MPhil

2020

James Daniel Hancock

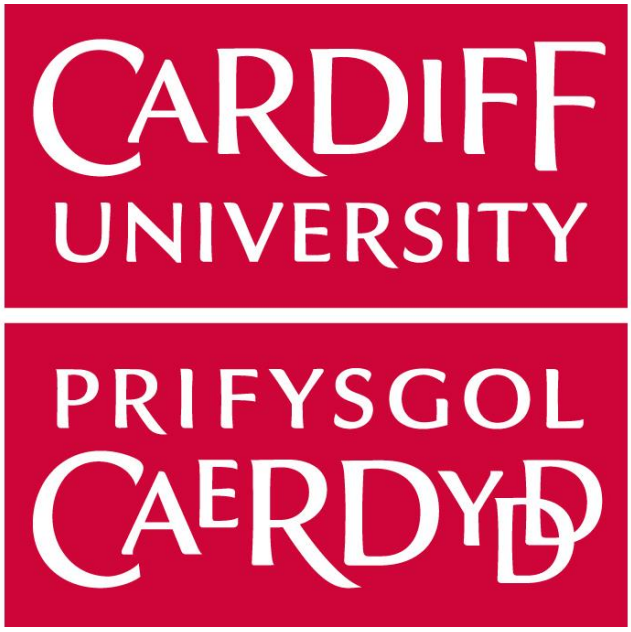

Acknowledgements

Firstly, I would like offer my unconditional thanks to my supervisor Dr Timothy Easun for the opportunity to undertake this research project and for all of his support and guidance throughout my time at Cardiff and for his unwavering support, advice and understanding upon making the difficult decision to finish my PhD prematurely.

Secondly, I would like to offer thanks to all members of the Easun group, in particular Corey Jones, Alexander Tansel, Nimai Mehta and Luke Kidwell for all of their help training me. I would also like to thank my MChem student Joseph Alemzadeh and to acknowledge his help with characterising the non-extended linker in this report. I would also like to acknowledge and thank Alexander Tansell and Louisa Davis for providing me with the SEM images of the NOTT-100 crystals. Special thanks to Dominic Ward for helping me with synthesis and for his friendship and good sense of a humour.

I would also like to thank all the other PhD and MChem students of the Easun Research Group for their support and companionship throughout my time amongst them. Whilst working within the laboratory, members of the group provided helpful insight into our field of research and gave many helpful ideas for the work I was undertaking.

Finally, I would like to thank all of those in the reading room of 2.72 and laboratory 2.84 of Cardiff University's Main Building, you have all made this year very enjoyable.

Abstract

This work is divided into two thematic sections. The first details the synthesis of two photo-active linkers and the attempted synthesis of MOFs containing the photoactive linkers to form functional materials. It also discusses the synthesis of the amorphous material AN64, as well as discussing the detailed characterisation of this material. The second section studies the size of NOTT-100 crystals after synthesis and after exchange with 12 different common lab solvents both before and after SEM imaging and studies the size distribution of particles in order to assess the environmental stability of these MOF crystallites.

Part 1

A photoactive spiropyran core and two photo-active linkers were synthesised. In summary a series of combinatorial reactions were performed with the extended and non-extended photo-active linker in DMF, and a zirconium-based material was synthesised, but even when lower temperature combinatorial synthesis was performed no crystals large enough for single crystal X-ray diffraction formed.

After altering both the modulator and temperature the solvent was changed. DEF was used instead of DMF in a series of combinatorial reactions with the non-extended linker, but a crystal of suitable quality did not form. Combinatorial synthesis was performed with aluminium, gallium and gadolinium and amorphous gallium and gadolinium-based materials were synthesised. Detailed characterisation of AN64 was performed. AN64 was found to be thermally and mechanical stable. The thermal stability of AN64 was studied and the resulting TGA mass loss graph appeared to show two overlapping decay curves which could indicate that two different solvent binding sites are present in AN64. A cycled TGA experiment showed AN64 was able to reversibly adsorb and desorb atmospheric water.

Part 2

Part 2 studies the size of NOTT-100 crystals after synthesis and after exchange with 12 different common lab solvents both before and after SEM imaging. We have developed a straightforward procedure for extracting particle size distribution from both optical and SEM images. In this study the SEM measurements were not innocent. The more polar and higher acceptor number solvents, even when only present in residual amounts after air drying, are enough to break up the crystallites when they are exposed to vacuum, however, there was no apparent correlation between solvent surface tension, vapour pressure and boiling point and the particle size distribution. There was no apparent trend between the secondary exchange solvent and the particle size distribution in the optical images of the crystals, prior to the SEM measurement.

Table of Contents

1. Introduction

1.1 Metal-Organic-Frameworks

Metal-organic frameworks (MOFs) are a class of porous polymeric material, consisting of metal ions which act as nodes (also known as secondary building units, or SBUs) linked together by organic bridging ligands, as shown in Figure 1.[1] Due to their structural and functional tunability, the area of MOFs has become one of the fastest growing fields in chemistry.[2] This new class of material now consists of around 70,000 frameworks produced within the past 30 years, showing the rapid exploration of the field.[3]

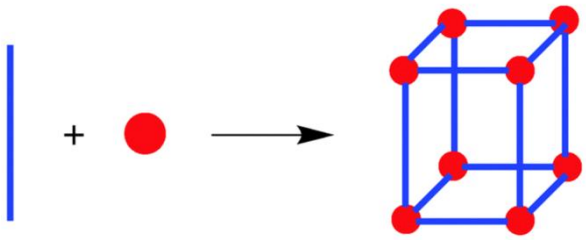

Figure 1: The formation of a MOF from metal ions (red) and organic bridging ligands (blue).

The hallmark of MOFs is their potential porosity. MOFs porosity is due to the fact that MOFs are stable in the absence of a guest molecule. MOFs with surface areas that exceed BET values of 6000 m^2g^{-1} have been reported.[4] When characterising porous materials surface area is one the most important quantities to consider. "BET analysis is the standard method for determining the surface area of a material and it from nitrogen adsorption isotherms and was originally derived for multilayer gas adsorption onto flat surfaces."[5] BET analysis provides a measure of surface area by the adsorption of nitrogen as a function of relative pressure.

MOFs offer great flexibility in terms of structures and properties available. MOFs contain both organic and inorganic structural building units and they can be modified both before and after synthesis.[6] This flexibility means MOFs have a great potential for applications in gas storage,[7–9] separation,[10–12] drug delivery,[13–15] biomedical applications,[16–19] sensing[20–23] and catalysis.[24–27] In this project, one of the target applications is water purification.

1.2 Synthesis of MOFs

Many different techniques can be used to synthesise MOFs. Different synthetic techniques can afford a wide variety of structural morphologies, for instance different MOF synthesis can involve sonochemical, microwave-assisted, electrochemical and conventional heating methods.[28]

The most common way to synthesise MOFs is by using solvothermal synthesis. This process involves reacting metal salts and organic linkers dissolved in a suitable solvent that is then heated (often using a hotplate or an oven) inside a screw top vial or sealed pressure vessel above the solvent's atmospheric boiling point.[29] Sealing the vessel generates autogenous pressure to reach higher temperatures enabling the self-assembly process in solution to form larger macromolecules.

The use of modulators in MOF synthesis is a common way to prevent rapid formation of amorphous material. Farha *et al*. describe modulators as "non-structural, monotopic linkers (e.g. benzoic acid, acetic acid, hydrochloric acid), which can form dynamic bonds with the metal precursor and help to slow down the formation of structural bonds by competing with the linkers for metal coordination sites."[29] Modulators can be added during the MOF synthetic procedure and they can alter the growth rate of the crystals formed.[30] Modulators affect MOF synthesis by altering the equilibria between the binding forms of the starting materials and the non-binding forms affecting the rate at which organic linkers can react with metal atoms, as shown in Figure 2.

$$RCOOH \rightleftharpoons RCOO^- + H^+$$

$\longleftarrow$

Addition of acid

Figure 2: The equilibria of carboxylate moiety in solution and how it is affected by the addition of acid

1.3 MOF crystallinity and crystal size

The size of MOF crystals can be very important for stability and functionality,[31,32] as well as for allowing characterisation by single crystal X-ray diffraction. Several efforts to control the size of MOF crystals have been made.[33] Wang *et al.* have demonstrated a facile strategy for precisely controlling the crystal size of several MOFs by separating the MOF nucleation and growth processes.[34] They achieved this by adding small amounts of metal precursor to the organic ligand solution before the rest of the metal precursor was introduced. The small amount of metal ions interact with the organic ligand to form clusters, which act as the seeds for later crystal growth. Changing the amount of pre-added metal precursor directly affects the size of the resulting crystals.[34]

The size of MOF crystallites can strongly affect the catalytic function of a MOF.[35] Phan *et al.* have reported using MOF-5 as an efficient heterogeneous catalyst for Friedel–Crafts alkylation reactions.[35] The synthesis of MOF-5 is outlined in Figure 3.

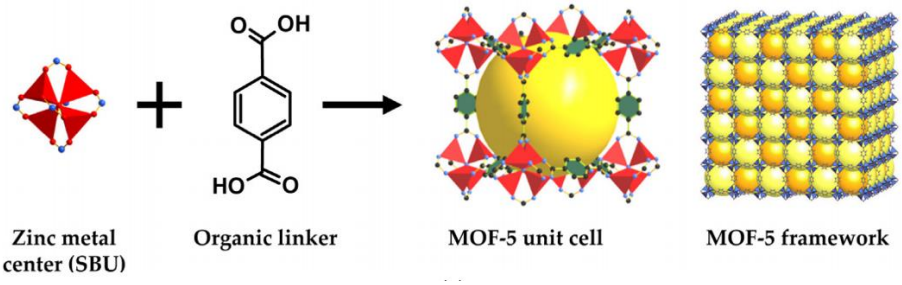

Figure 3: Synthesis of metal-organic framework 5 (MOF-5) from a Zn metal cluster and cluster and terephthalic acid (reproduced from Perez *et al.*).[36]

Using scanning electron microscopy (SEM) they observed high quality cubic crystals with crystal sizes ranging between approximately 100 and 200 μm. In later work Ahn *et al*. investigated the effect of particle size variation on guest sorption and catalytic activity of Co-MOF-74, observing a marked difference in water uptake between samples made solvothermally or via microwave synthesis.[37] The synthesis of MOF-74-Co is outlined in Figure 4. Like Phan *et al.* they characterised particles sizes by SEM. The size of MOF crystallites is directly related to the external surface area to volume ratio.

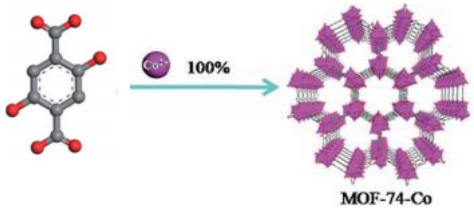

Figure 4: Synthesis of MOF-74-Co (reproduced from Chen *et al.*).[38]

SEM is a very common technique used to visualise MOFs.[39–41] Over 100,000 articles using SEM to study MOFs have been published.[42] SEM scans a sample with a focussed beam of electrons. The resulting image derived from the electron-sample interactions reveals information about the sample including morphology and particles size, although these are often reported qualitatively. There is no standardised approach in the field to quantitively assess particle size distribution from such images, although issues around voltage selection and sample counting are well discussed in literature.[29] Other similar techniques such as transmission electron microscopy (TEM) have been used to image MOFs.[43] However, the electron beam used in TEM can damage the MOF sample, resulting in a degradation of the framework structure.[44] Dynamic light scattering (DLS) is another primary method used to measure particle size distribution. DLS has the advantage of observing many particles at once, but DLS is typically limited by factors such as the optical configuration of the instrument, laser wavelength and detector sensitivity.[45]

In the later part of this thesis (Section 2.4) we have investigated the use of SEM in sizing MOF crystallites.

1.4 Photo-activity in MOFs

Methods for the incorporation of light-responsive groups within MOFs include the use of pendent groups pointing into the pores,[46] and the filling of pores with light-responsive guest molecules.[47] The light-responsive groups within these materials may then alter their conformation when irradiated at a specific wavelength of light. One aspect that makes MOFs interesting is their variable pore size. Being able to alter this pore size can enable MOFs to be used in a wide range of applications.[48]

It is also worth considering light penetration in MOFs. Zhou *et al.* functionalised MOF-5 with a photo-active azobenzene group which enabled the reversible alteration of guest molecule adsorption upon photochemical treatment. However, they noted that it was difficult for photons to penetrate into the core of the crystals because of scattering from defects and absorption from competing chromophores.[47] Gascon *et al* also noted that “in addition to molecular design, crystal engineering can be an essential tool to improve the efficiency in the incident photons' usage. Light penetration could be in principle enhanced by increasing the surface to volume ratio of the MOF's particles”.[49]

Photo-crystallography is a technique used to determine the full three-dimensional structure of a photo-active molecule. The crystal must be large enough to analyse but it must also be small enough to allow photons from the optical source to pass through the whole of the sample so that uniform photo-activation is realised.[50]

1.5 Spiropyrans and their incorporation into MOFs

Spiropyrans consist of an indoline and chromene (benzopyran) moiety which are bound covalently at the C_1 atom, shown in Figure 5. Spiropyrans emerged in the 1950s when Hirshberg reported the optical transitions between the ground and excited states of a series of spiropyrans that were characterised by UV-visible absorption spectroscopy.[51]

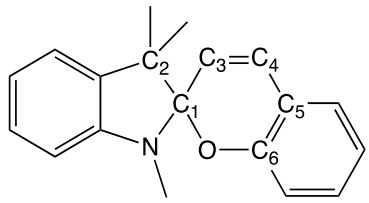

Figure 5: Structure of a general spiropyran, where the C_1 carbon atom refers to the carbon atom in the spiro-position.

When spiropyrans are irradiated with UV light the C_{spiro}-O bond can break/form, which allows switching between a closed and open form (Figure 6).[52] The excitation of electrons from bonding to anti-bonding orbitals due to the absorption of UV light weakens this C_{spiro}-O bond, enabling the dissociation of this bond. The dissociation of

this bond initiates a ring-opening reaction that converts the closed spiropyran (SP) into the open merocyanine (MC) form. The MC form can spontaneously undergo a ring closing process, enabling the regeneration of the SP form. The MC to SP back-conversion can be promoted thermally or by visible light.[53] It is also worth stating that the addition of strong base can cleave the C_{spiro}-O bond.

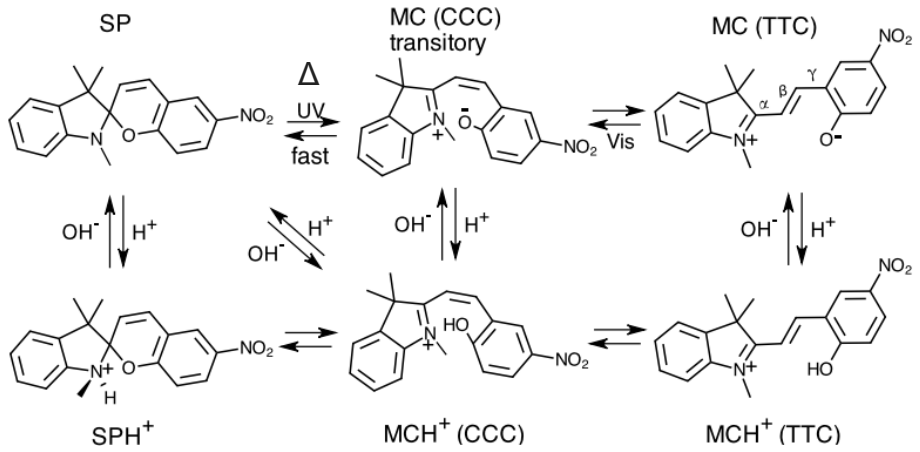

Figure 6: Various conformations of a spiropyran in solution undergoing ring opening and then cis-/trans- isomerisation into the merocyanine forms. The acronyms CCC and TTC stand for the α, β and γ carbon positions being *cis-/trans-* relative to each other (reproduced from Markworth *et al.*).[54]

Kinetic studies performed on spiropryans highlight the ease at which these molecules can switch between their spiropyran and merocyanine forms. Interconversion timescales are highly situation-dependent (solvent, substituents, irradiation conditions) and range from ps-timescales for bond breaking and conformational reorganisation through to minutes or hours for thermal back-conversion.[55]

Applications which use the spiropyran's ability to act as a 'photo-switch',[56] include incorporating spiropyrans into the synthesis of biomolecules, nanoparticles and also the surfaces of solids to produce photodynamic materials.[57–59]

To date, there have been two examples of a spiropyran being incorporated into a MOF.[60,61] The first example involved a spiropyran (SP) moiety being incorporated into a MOF as a pendent group via post synthetic modification of a modified MOF-808 framework. The synthesis of MOF-808 is outlined in Figure 7.

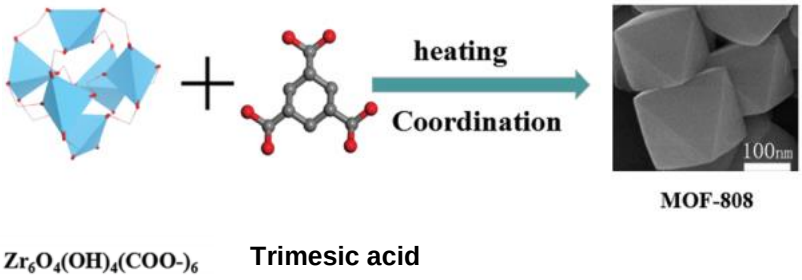

Figure 7: Synthesis of MOF-808 (reproduced from *Xu et al.*).[62]

When MOF-808 was modified with the SP moiety a decrease in the surface area from 1201 m^{-1} g^{-1} to 836 m^{-1} g^{-1} was observed. MOF-808-SP showed a photoresponsive BET surface area, pore volume and CO_2 uptake. This demonstrates a potential for light dependent low energy gas separation and/or storage. Shustova *et al.* synthesised two novel linkers with a spiropyran group attached to the ligand backbone, as shown in Figure 8.

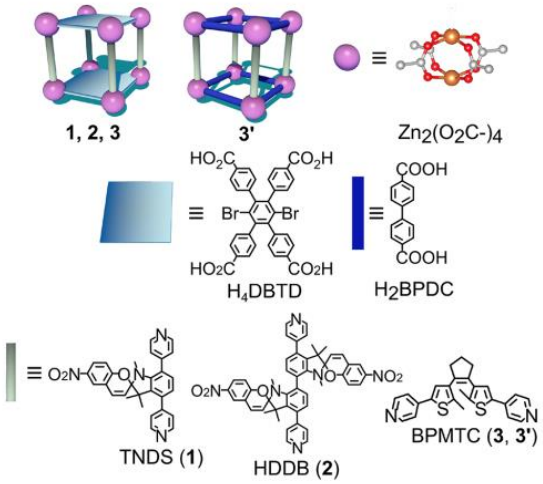

Figure 8: The linker TNDS, HDDB, and BPMTC linkers used by Shustova *et al* to form a spiropyran containing MOF. Orange, red, teal, and grey spheres correspond to zinc, oxygen, zirconium, and carbon atoms, respectively (reproduced from Shushtova *et al.*).[60]

These linkers were then used to form two novel MOFs where they acted as pillar linkers. The photoisomerisation rate of the spiropyran could be tuned as a function of framework structure.[60] The incorporation of the photoresponsive spiropyrans within the rigid MOF enabled the control the cycloreversion kinetics, with a level of control that is not accessible in the packed molecular solid state or solution. Shustova *et al.* were also able to achieve complete isomerization for coordinatively immobilized

spiropyran derivatives, which typically exhibiting limited photo-switching behaviour in the solid state. This was typified by a photoisomerization rate of 0.16 s^{-1} (typical for cycloreversion in solution) for the novel monosubstituted spiropyran derivative grafted to the backbone of the MOF pillar.[60]

These two examples provide an important proof-of-concept example of the photoresponsive nature of spiropyran-functionalised MOFs, leading the way towards other framework platforms that may also exhibit light modulated properties.

1.6 The global water shortage

Approximately 1.1 billion people worldwide lack access to water, and a total of 2.7 billion find water scarce for at least one month of the year.[63] By 2025, two-thirds of the world's population may face water shortages.[63] The Earth contains about 1.4 x 10^9 km^3 of water and about 97.5% of this is salt water.[64] Water desalination could be the answer to these water scarcity problems.

Well-established desalination technologies can be classified into two categories, thermal (phase change) and membrane (non-phase change) processes. Thermal processes consist of an evaporator and condenser to vaporise freshwater from the feedwater (seawater or brackish water). Membrane processes use a physical barrier such as a membrane to separate the dissolved salts from the feed water by mechanical or chemical/electrical means using a membrane separator between the feed and product water.[65] There are concerns about the potential environmental impacts of large-scale seawater desalination plants, as large amounts of thermal energy are required for thermal desalination process.[66] Most of this thermal energy comes from burning fossil fuels, resulting in large scale CO_2 production.[67]

1.7 MOFs and desalination

Li *et al*. prepared a zirconium-based MOF (UiO-66) that was fabricated onto alumina hollow fibres.[68] The synthesis of UiO-66 is outlined in Figure 9.

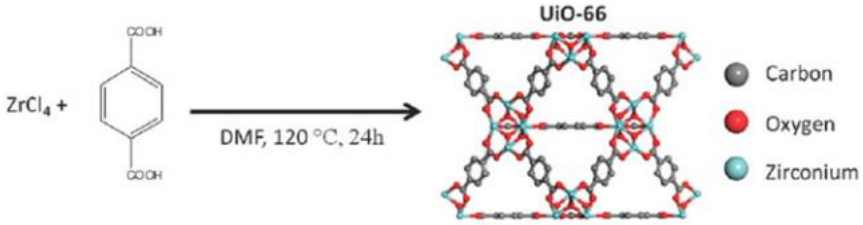

Figure 9: Synthesis of UiO-66 (reproduced from *Sun et al.*).[69]

The membrane was subject to 100 days of continuous stability testing under hydrothermal conditions. PXRD experiments showed that even after 100 days of testing, good crystallinity of UiO-66 samples was retained. The desalination potential for this material was tested by studying the membrane's ion rejection properties. It was hoped that the membrane would allow the permeation of water, but not the permeation of the ions present in solution. The desalination studies showed that group 2 metal ions (Ca^{2+}, Mg^{2+} and Al^{3+}) were well rejected (≥ 90% rejected in all cases), but potassium and sodium ions were less well rejected (47% and 46%, respectively). This difference in ion rejection capabilities was thought to be due to the ligand dynamics of UiO-66 as its carboxylate groups can change their coordination mode from edge-bridging to monodentate. It could also be due to missing-ligand defects in the MOF.[70]

Wang *et al*. also synthesised a UiO-66 membrane that was fabricated onto porous ceramic hollow fibre substrate.[71] In an effort to reduce the cavity size in the UiO-66 based material, they performed post synthetic defect healing (PSDH) and replaced benzenedicarboxylate with 2,5-dihydroxybenzenedicarboxylate. The extra hydroxy groups helped to reduce the aperture size. Ion rejection tests were performed on the original material and PSDH modified material. Interestingly PSDH was found to increase the membranes' Na^+ rejection rate by 75% (an increase from 26% to 45%). Both Wang *et al*. and Li *et al*. have thus demonstrated how MOFs can desalinate water,[71,72] but they have also highlighted the difficulties in separating sodium ions in particular.

A previous member of the Easun group, Dr Adam Nevin, was able to synthesis a photo-active spiropyran-containing material which called AN64 (discussed in more detail in section 1.8) which showed promising desalination potential. Dr Nevin flowed a solution which contained water and sodium ions through a transparent narrow column (~2 mm internal diameter) which contained AN64 and he measured the conductivity of the solution after passing through the column. A reduction in conductivity indicates a reduction in the concentration of sodium ions present. When AN64 was radiated with UV light it was noted that the conductivity of the solution decreased; this was interpreted as the irradiation of AN64 with UV light enabling the formation of the merocyanine form of the spiropyran, and this zwitterionic form could then coordinate to small cations effectively capturing these ions.

1.8 Project aims

The initial aim is to synthesise photo-active spiropyran-containing linkers. These photo-active linkers can then be utilised in combinatorial synthesis to form MOF frameworks which contain the linkers. Spiropyran linkers were chose because if a spiropyran can be incorporated into the struts of a stable framework, irradiation of the photoresponsive groups could cause the formation of the merocyanine forms. These zwitterionic linkers could then coordinate to small cations effectively capturing these ions. These particular spiropyran linkers where chosen as their synthetic pathways have been explored by previous students working with Dr Easun. These linkers also contain benzene groups which should add some structural rigidity to these often conformationally unstable molecules, potentially making their incorporation into MOFs easier. The use of larger and hence more flexible linkers such as the extended linker discussed in section 2.1 may make accommodating the spiropyran central bend and conformational variability into known MOF topologies more feasible, which in turn may enable the formation of large crystals which would allow characterisation of these materials via single crystal x-ray diffraction.

A former member of the Easun group, Dr A. Nevin, was able to incorporate a spiropyran based linker called **L1** (shown in Figure 10) into a zirconium-based amorphous material (called AN64).

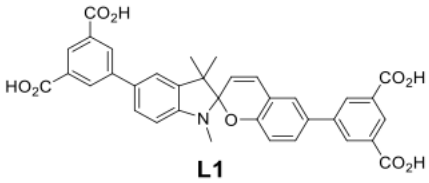

Figure 10: The spiropyran linker present in AN64.

This material was found to be water stable, and desalination tests showed encouraging preliminary results for sodium cation removal from a saline sample. A second aim is to better characterise AN64, to gain a greater understanding of this material and its desalination potential, as well as gaining a greater understanding of the stability of this material. This material is very interesting, however, it would be more desirable to form a highly crystalline material such as a MOF. Having a crystalline material instead of an amorphous one would make detailed structural characterisation simpler.

The second part of this thesis involves studying and assessing the size and stability of MOF crystals. The main aim of Section 2.4 is to investigate how altering the secondary exchange solvent used during the washing of NOTT-100 crystals affects both crystal size and stability. A second aim is to develop a straightforward procedure for extracting particle size distributions from both SEM and optical images of the NOTT-100 crystals.

2. Results

2.1 Linker synthesis

A spiropyran core (**SP**) and two photo-active linkers have been synthesised (**L1** and **L2**) following established procedures in the research group (see experimental).

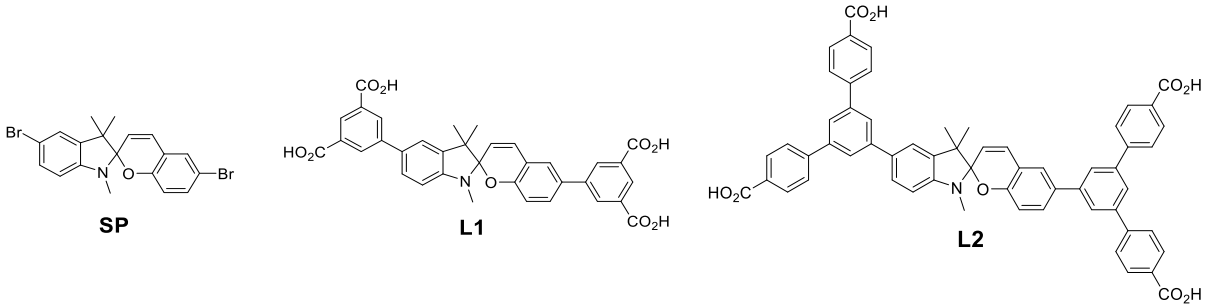

Figure 11: The spiropyran core (**SP**) and the two photoactive linkers (**L1** and **L2**)

Full experimental details can be found in the experimental section. Initially the spiropyran core (**SP**) was synthesised (Figure 12). This involved reacting 5-bromo-salicylaldehyde and 1,3,3-trimethyl-2-methyleneindoline which produced the photoactive core for the linker. A resonance form of the indoline compound allows for the nucleophilic attack of the aldehyde group. After proton transfer from the alcohol a ring-closing mechanism occurs which forms the C_{spiro} atom. The elimination of a water molecule forms the double bond of the spiropyran. The resulting spiropyran molecule was brominated using N-bromosuccinimide (NBS) to form **SP**. Bromination occurred on the atom para- to the nitrogen of the indoline ring. The reason that bromine binds para- to the nitrogen is due to the inductive and mesomeric effects occurring in the resonance structures of mono-bromo **SP**. Hence this position is the most active towards electrophilic substitution. Other spiropyran derivatives have been reported to brominate in equivalent positions.[73]

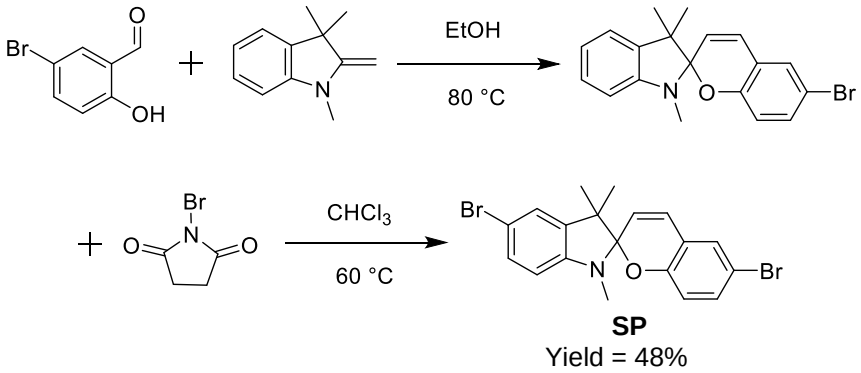

Figure 12: The synthetic route to make **SP**.

By utilising a Suzuki-Miyaura cross coupling reaction, **SP** was coupled to an isophthalate boronic acid to form the ester-protected precursor to **L1** (see Appendix 1 for details on the catalytic mechanism). The carboxylate sites of the boronic acids were protected with ester groups (see experimental for synthetic procedure for making the protected-isophthalate boronic acid) so that the acid sites did not react prematurely (Figure 13). Once coupled to the spiropyran core the organic linker was deprotected via hydrolysis using a trimethylsilanolate salt which removed the ester groups to yield **L1**. Potassium trimethylsilanolate was chosen as the base for the hydrolysis due to its mild electron donating capabilities – if a stronger base such as sodium hydroxide were used the photoactive core may have been cleaved.

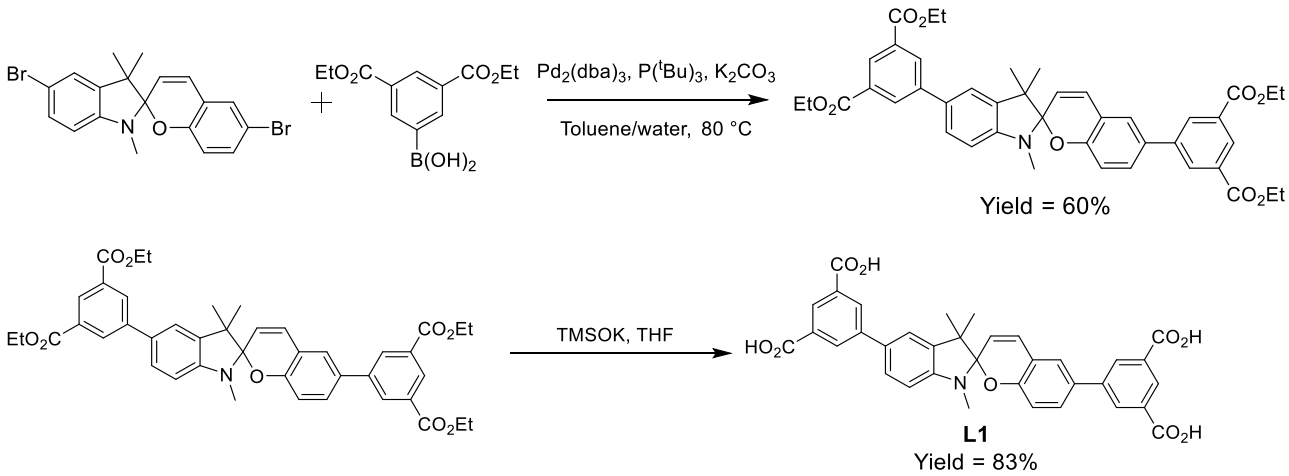

Figure 13: The synthetic route for **L1**.

The synthesis of **L2** required an extended boronic acid to be synthesised (Figure 14). This was achieved by reacting a dibromo-boronic acid with 1,8-diaminonapthalene (DAN). This condensation reaction formed a DAN-protected dibromo-boronic acid. A

Suzuki-Miyaura cross coupling reaction was then used to couple the DAN-protected species with an ester-protected para-carboxylate boronic acid to form a DAN-protected extended boronic acid. The DAN group was then removed from the boronic acid using sulfuric acid.

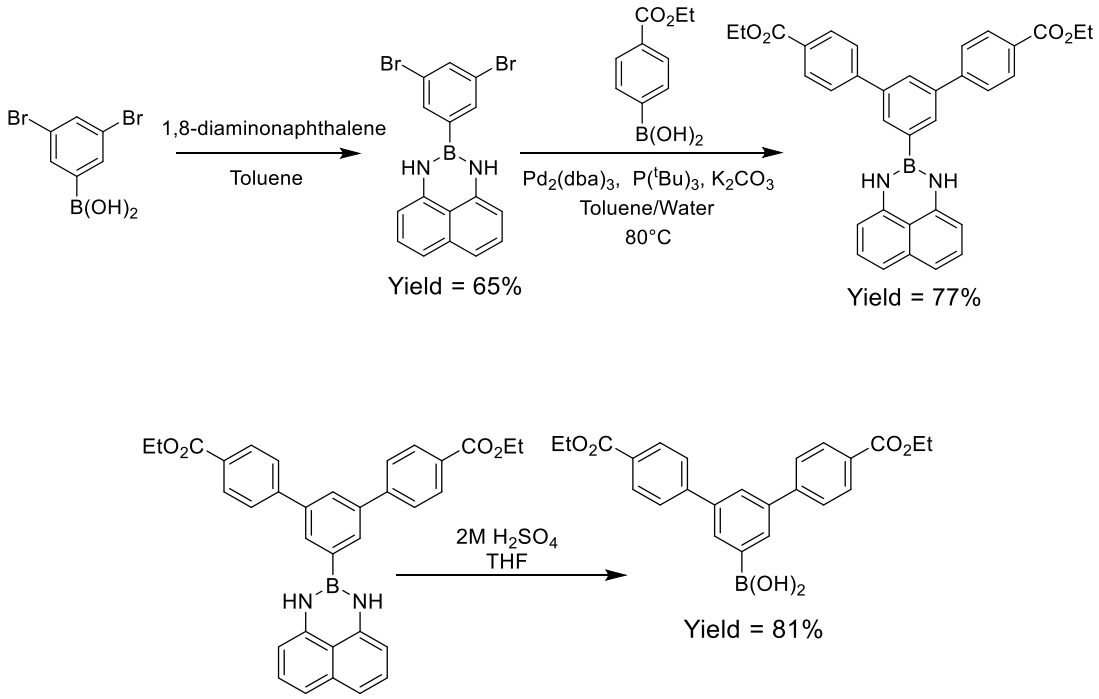

Figure 14: Synthesising the extended boronic acid.

The extended ester-protected boronic acid was then coupled with **SP**, again using a Suzuki-Miyaura cross-coupling reaction (Figure 15). Analogously to the deprotection in the synthesis of **L1**, a trimethylsilanolate salt was used to remove the ester groups.

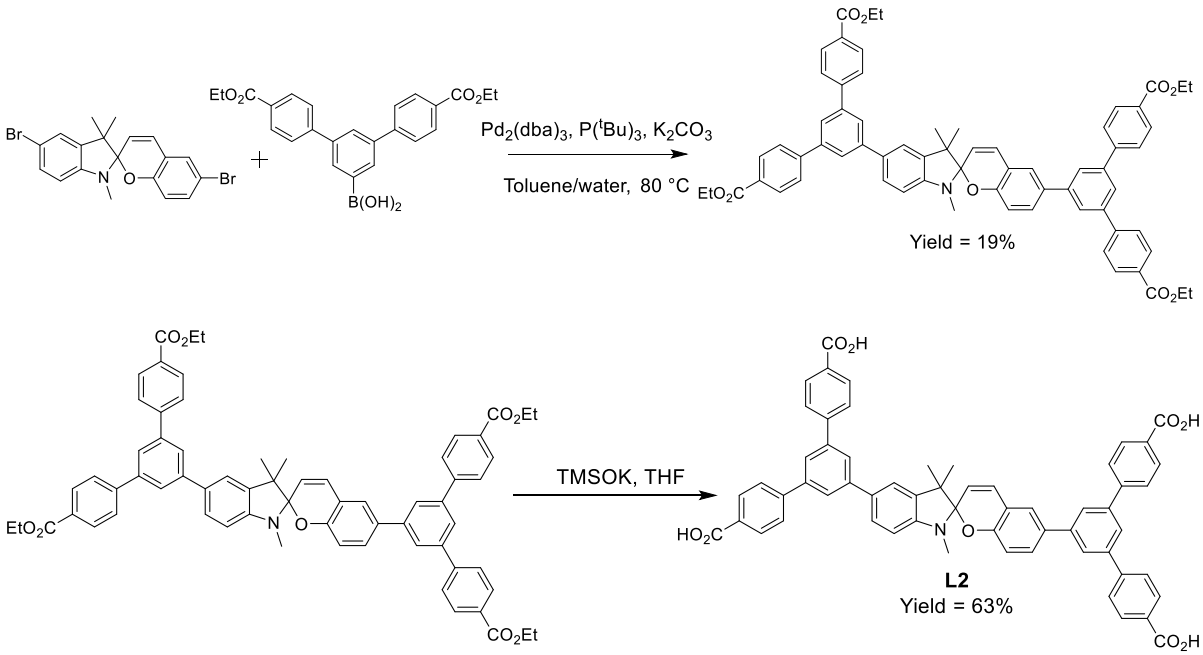

Figure 15: The synthetic route for **L2**.

2.2 Combinatorial syntheses

MOF synthesis was attempted using a combinatorial approach. Typically, the spiropyran linker and a metal salt were dissolved in a suitable solvent such as dimethylformamide (DMF). DMF is a suitable solvent as it has a high boiling point and it is highly miscible with other solvents, such as water. In most cases a modulator was added to the reaction. Modulators can alter the growth rate at which crystals are formed, which could be a key factor in deciding whether the reaction forms the thermodynamic product or kinetic one(s).[30,74,75]

All initial combinatorial experiments were performed using zirconium chloride as the metal salt. Zr(IV) ions can form strong coordination bonds with the carboxylate groups of **L1** and **L2** due to hard-acid hard-base interactions. These strong interactions enable known Zr-MOFs to exhibit good chemical and thermal stabilities.[68,76] The mass of linker, metal, temperature, length of time heating, the solvent and its volume used in the initial combinatorial reactions were based on previous work performed by Dr Nevin. He found conditions that led to the formation of an amorphous water-stable zirconium spiropyran-based material. My first set of combinatorial reactions (combinatorial 1) used these quantities and conditions but altered the amount and type of modulator used (Appendix 1). Altering the modulator can facilitate the formation of a crystalline

material, instead of an amorphous one. Dr Nevin formed solid material successfully using hydrochloric acid (HCl) and nitric acid (HNO_3), therefore different amounts of these two acids were added separately to the combinatorial vial. Each vial contained 10 mg of **L1**, 25 mg of $ZrCl_4$, 1 ml DMF. The vials were all heated at 60 °C for 3 days. Of the sixteen combinatorial synthesis twelve formed enough solid to enable characterisation via powder X-ray diffraction (PXRD). Five of these vials contained crystalline material (Figure 16). None contained crystals large enough for single crystal X-ray diffraction (SCXRD).

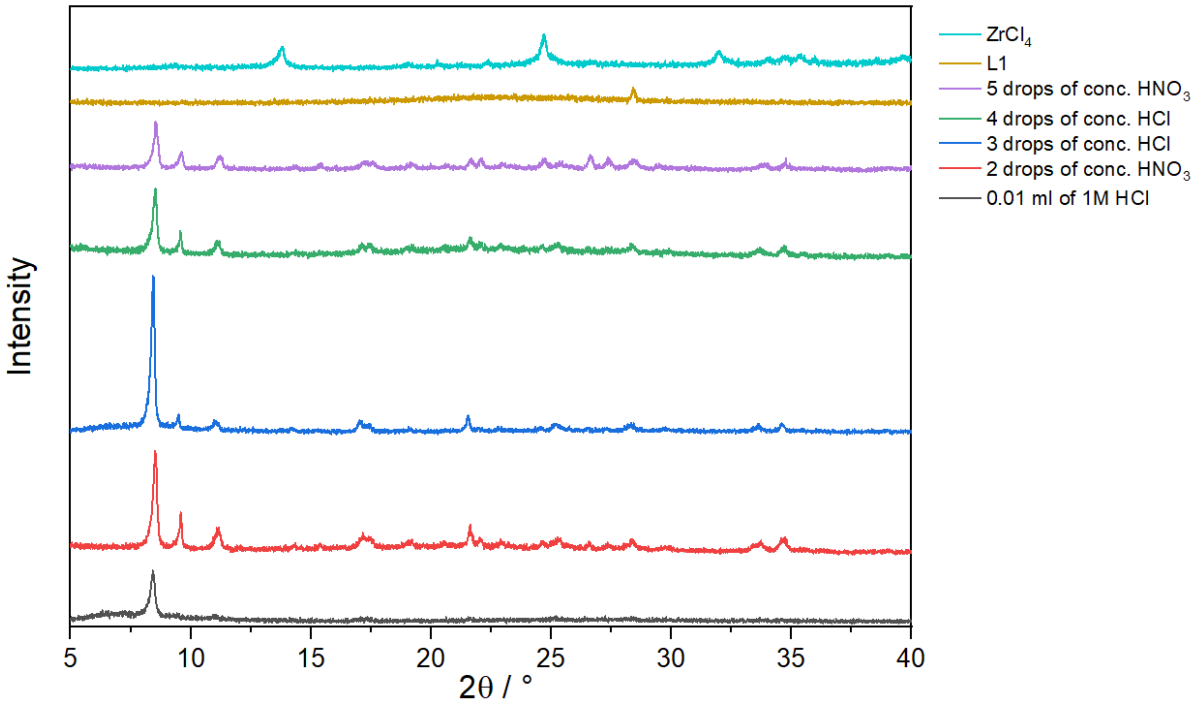

Figure 16: The PXRD patterns for the most promising samples from combinatorial 1, each colour represents an experiment where a different modulator was used.

In Figure 8 all the PXRD patterns exhibited a high intensity peak at approximately 8.5º 2θ. This equates to a *d*-spacing of *ca*. 10.5 Å. This d-spacing is larger than typically found in a simple metal salt. However, this length is smaller than the length of unbound **L1,** approximately 16.5 Å. It is worth stating that these *d*-spacing arise from layers in the structure of the material and in MOFs this is often related to the linker length. It was unclear if **L1** is present in the solids that were synthesised. To test if a simple metal salt was forming a series of control experiments were run (combinatorial 2 and 3 can be seen in the Appendix). The control experiments involved performing a reaction without the linker or without $ZrCl_4$ at both 60°C and 70°C for 3 days. No solid

formed in these control experiments, which initially suggests that both the linker and $ZrCl_4$ are required to form the crystalline material observed in combinatorial 1. The PXRD pattern for $ZrCl_4$ exhibits high intensity peaks at 14, 25 and 32º 2θ (as shown in Appendix 3). Interestingly, none of the PXRD patterns displayed in Figure 16 show any of these peaks, suggesting the simple $ZrCl_4$ salt is not present in the synthesized material.

After the success of combinatorial 1 different modulators were used whilst keeping the rest of the reaction conditions the same. Alongside several different acids which are commonly used as modulators in MOF synthesis, L-proline was also used (combinatorial 4 in the Appendix). Amino acids can act as highly efficient modulators for zirconium MOFs,[30] which can lead to increased particle sizes, some of which are suitable for SCXRD.[77] The vials were heated for 60°C for 3 days; after 3 days every vial contained solid material. Only four contained crystalline material (Figure 17). As for the PXRD patterns in combinatorial 1, there was an intense peak at 8.5º 2θ in all four cases, but the particles were still too small to analyse using SCXRD.

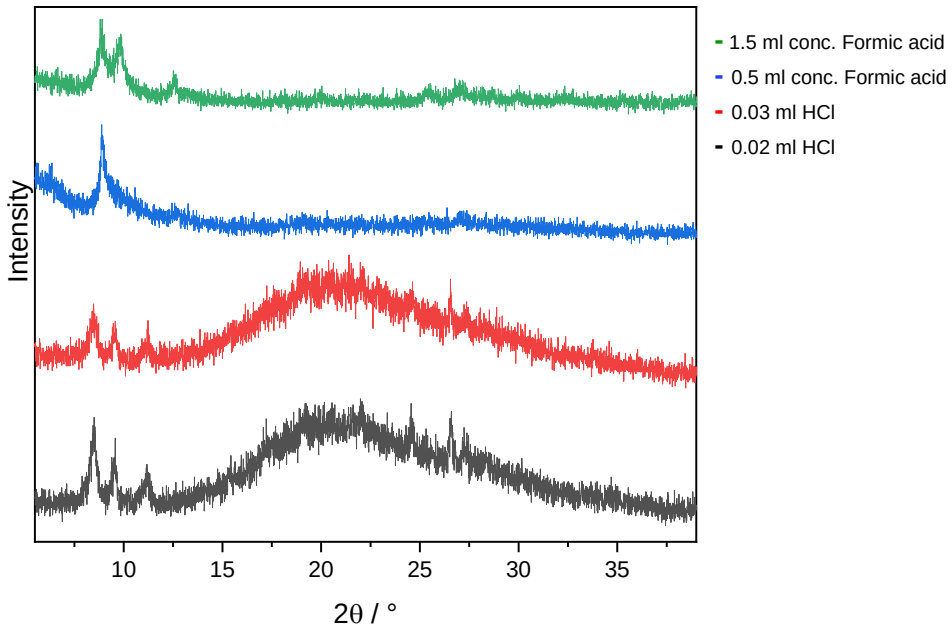

Figure 17: The PXRD patterns for the crystalline samples from combinatorial 4, each colour represents an experiment where a different modulator was used.

The experiments from combinatorial 4 were repeated at the lower temperature of 50 °C (combinatorial 5). A lower temperature was used to slow down crystal growth in

order to obtain larger crystals. After three days of heating, solid was observed in every vial, but only two contained crystalline material (Figure 18). Neither sample contained a crystal of suitable quality for SCXRD. Ideally, a crystal of a few tens of micrometres to a few hundred micrometers would have been obtained

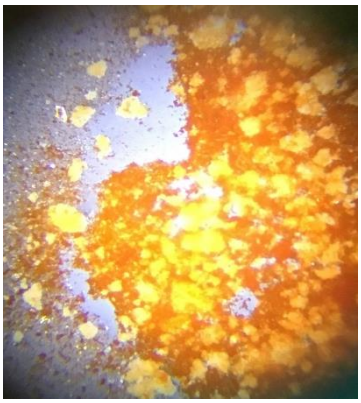

3 drops of conc. HCl

Proline 260 mg and conc. HCl 0.004 ml

Figure 18: Optical images of the two vials which contained crystalline material (45x zoom).

After not forming crystals of suitable quality using **L1**, the extended linker **L2,** was used in series of combinatorial reactions. The conditions from combinatorial 5 were mimicked using the same solvent (1 ml DMF), mass of salt (25 mg $ZrCl_4$) and the same modulators but **L2** was used in place of **L1** (combinatorial 6). After 3 days of heating six vials contained solid. PXRD showed an intense peak at 8.5 º 2θ in the four samples which used HCl as a modulator. When the non-extended **L1** was used peaks at 8.5 º 2θ were also observed. The fact that this peak remained the same, even when a larger linker was used, implied that the linker was not being incorporated into this zirconium-based material, as if it were, we would have expected peaks at different positions as a result of different structures for the different sized linkers.

To test this hypothesis, a series of combinatorial reactions were performed with **L1**, **L2** and in the absence of linker (see Appendix combinatorial 7). After 3 days of heating every vial contained solid and PXRD showed an intense peak for every vial at 8.5 º 2θ (Figure 19). This suggests that both **L1** and **L2** are not being incorporated into the zirconium-based material that is forming.

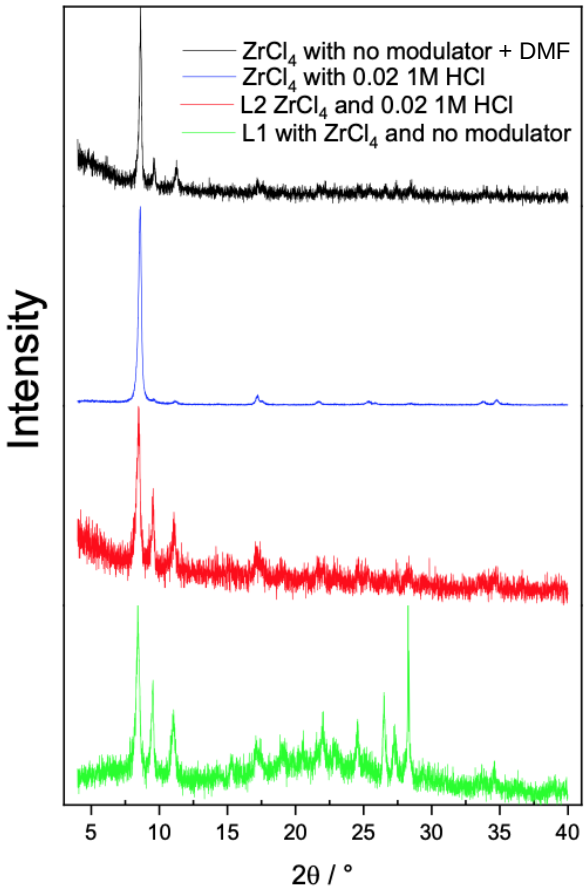

Figure 19: Selected PXRD patterns for the control reactions from combinatorial 7. Each colour represents an experiment where a different modulator was used.

After altering both the modulator and temperature the solvent was changed. Instead of DMF, the bulkier analogue, diethylformamide (DEF), was chosen. The electron-donating power of DEF is greater than DMF due to it having more electron-rich substituent groups bound to the nitrogen atom, allowing the basic solvent to coordinate more strongly to Lewis acidic sites. DEF should stabilise any growing frameworks by occupying the larger pores more effectively than the smaller DMF molecules and interacting strongly with the metal nodes to retain the crystal's structural integrity. **L1** was the chosen linker and HCl was the modulator. Half of the combinatorial vials were heated at 50 °C and the other half at 40°C (combinatorial 8 in the Appendix). Lower temperatures were used to slow down crystal growth in order to obtain crystals. After heating for 10 days solid had formed in all vials. Crystalline material had formed in all of the samples ran at 50 °C; PXRD showed an intense peak at 13.7º 2θ which equates

to a *d*-spacing of 6.5 Å (Figure 20), this is different to the peak at 8.5º 2θ when DMF was used. All the combinatorial synthesis run at 40°C contained only amorphous material.

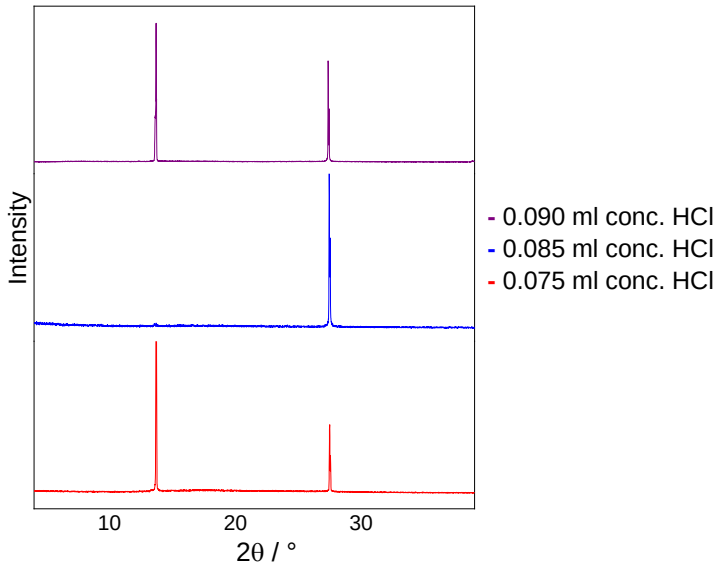

Figure 20: Selected PXRD patterns for the zirconium-based reactions from combinatorial 8. Each colour represents an experiment where a different modulator was used.

After the lack of success forming a MOF using zirconium, different metals were used in combinatorial synthesis. Three new metals were chosen: aluminium, gallium and gadolinium. These metals were chosen as they show no photoactivity in the UV-visible region of interest. The metal having little photochemistry of its own is advantageous. If a spiropyran is incorporated into a MOF the photoactivity will be due to the spiropyran linker, not the metal nodes. The three new metal salts (aluminium nitrate nonahydrate, gallium (III) nitrate hydrate and gadolinium (III) nitrate hexahydrate) were added in varying amounts with 10 mg of **L1** and 1 ml of DMF. The vials were heated at 60°C for 15 days (see combinatorial 9 Appendix). After heating none of the aluminium containing vials formed solid. However, when using a metal to ligand ratio of 1.3:1 gallium salt and 2.2:1 for the gadolinium salt an amorphous solid formed in each vial.

For the next set of combinatorial reactions, the two solid-forming reactions from combinatorial 9 were repeated (Appendix combinatorial 10). Differing amounts of modulator were added in order to grow crystalline material. After heating for 15 days at 60°C, solid had formed in each vial, but in each case the material was amorphous.

In summary a series of combinatorial reactions were performed with **L1** and **L2**, and a zirconium-based material was synthesised, but even when lower temperature combinatorial synthesis was performed no crystals large enough for single crystal X-ray diffraction formed. Combinatorial synthesis was performed with aluminium, gallium and gadolinium and amorphous gallium and gadolinium-based materials were synthesised.

2.3 AN64 characterisation

As mentioned previously, a former member of the Easun group, Dr A. Nevin, was able to incorporate a spiropyran-based linker (**L1**) into a zirconium-based amorphous material (called AN64). The synthesis of AN64 is outlined in Figure 21. This material was found to be water stable and desalination tests showed encouraging preliminary results for sodium cation removal from a saline sample. However, very little is understood about the structure of this material. A series of experiments were used to characterise and understand this unique material.

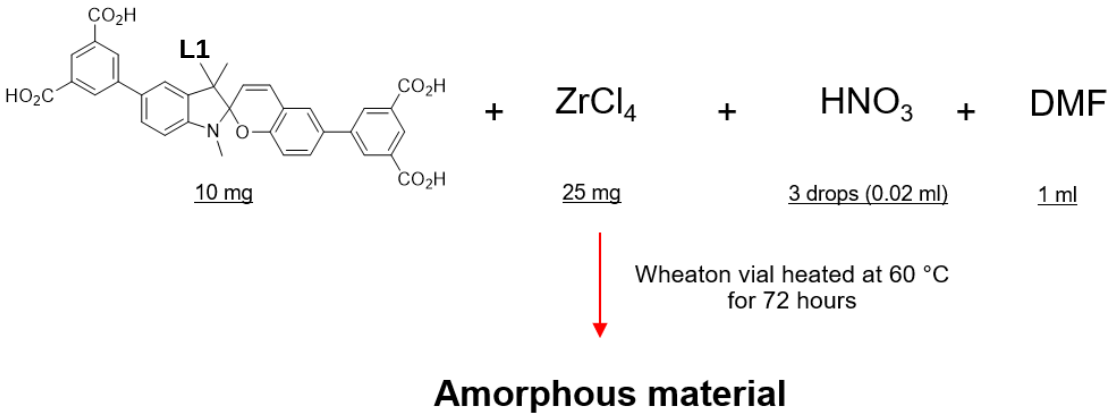

Figure 21: The synthesis of AN64.

Despite the large number of highly crystalline MOFs known, there is a subset of the MOF community studying amorphous metal-organic frameworks (aMOFs). These unique materials "retain the basic building blocks and connectivity of their crystalline counterparts, though they lack any long-range periodic order."[78] Amorphous MOFs combine the chemical versatility of MOFs with the unique properties of amorphous materials.[79] For instance, Cheetham *et al*. found that the amorphization of the Zr-based MOF UiO-66 led to a 15x slower release of pre-incorporated calcein when compared to crystalline UiO-66.[80]

AN64 was remade (the synthesis of AN64 is outlined in Figure 21) and a dark orange solid formed. To analyse AN64 further, it was ground with a pestle and mortar. The material was ground because a collaborator needed a fine powder sample to characterise AN64 using X-ray atomic pair distribution function theory (PDF). This technique can be used to study the local structure of amorphous materials at the atomic scale.[81] The material was also dried under vacuum at 50°C overnight. PXRD experiments were run on AN64 before being ground or dried; after being ground, and after being ground and dried (Figure 22). Promisingly, the powder pattern does not seem to have changed significantly after being ground and dried, suggesting that the material is stable and is able to withstand mechanical force.

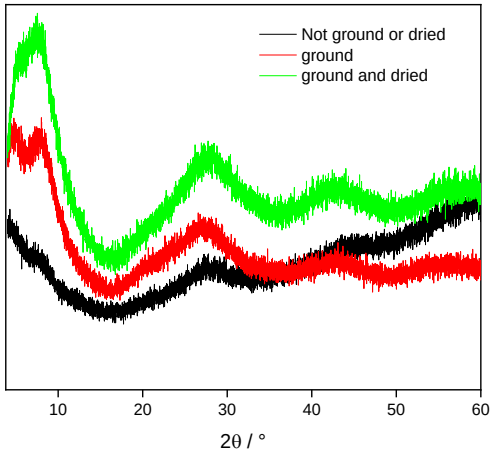

Figure 22: The PXRD patterns of AN64 before and after being ground and dried.

Next, the thermal stability of AN64 was studied using thermogravimetric analysis (TGA). A sample of AN64 was dried under vacuum and half was ground and the other half was not. These samples were then subject to TGA analysis (Figure 23). The overall shape of the TGA is similar, the only significant difference is the initial drop between 50-100 °C. This drop is not present when the material has been ground. The extra drop is probably due to weakly bound solvent or water molecules (from atmospheric moisture). The large mass drop at around 400°C can be attributed to thermal degradation of the linker. However, there is a mass drop present in both the ground and unground samples starting at around 190-200°C. This mass drop might due to solvent molecules which are bound inside AN64.

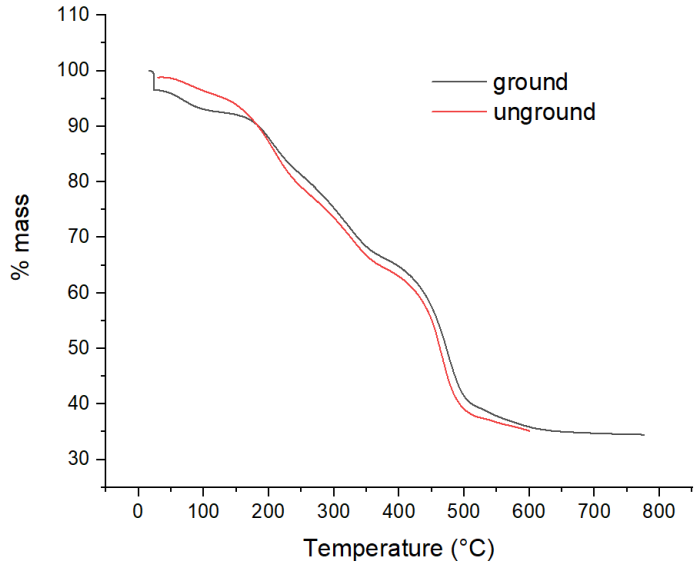

Figure 23: The TGA curves for a ground and unground sample of AN64.

Another TGA experiment was performed, but this time the dried and ground sample was held at 190 °C for 8 hours, enabling us to determine if this mass drop could be attributed to the loss of bound solvent (Figure 24).

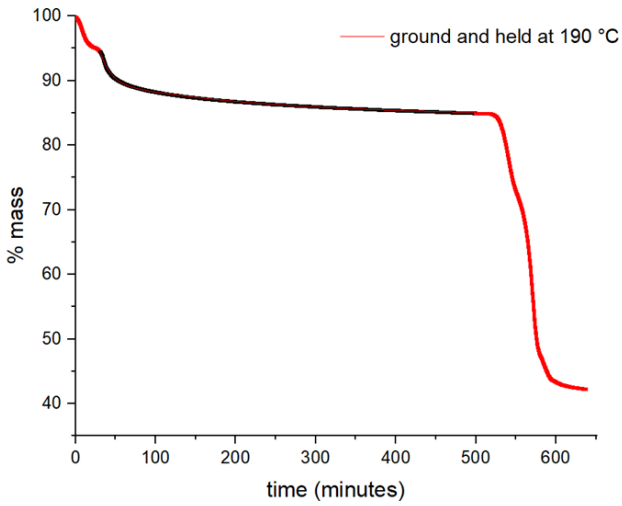

Model	ExpDecay2
Equation	y = y0 + A1*exp(-(x-x0)/t1) + A2*exp(-(x-x0)/t2)
Plot	% mass
y0	84.53407 ± 0.00258
x0	32.43135 ± 30663.48105
A1	4.25212 ± 10221.57375
t1	12.75583 ± 0.02347
A2	5.11907 ± 763.55238
t2	205.57673 ± 0.31535
Reduced Chi-Sqr	0.00321
R-Square (COD)	0.9988
Adj. R-Square	0.9988

Figure 24: The TGA curve and decay data for AN64 being held at 190 °C for 8 hours.

After 40 minutes 190 °C was reached. After being held at this temperature for 8 hours a mass loss of approximately 10% was observed. The black segment of the curve in Figure 16 indicates when the sample was held at 190°C. Interestingly, the decay can be fitted to the sum of two exponential curves, with decay lifetimes of 13 and 206 minutes. This could indicate that two different solvent binding sites are present in AN64 or that there is surface-bound and internal solvent. The latter possibility is unlikely given the noticeable mass loss below 190°C that is most readily attributed to external solvent loss.

Finally, we wanted to test if AN64 could be resolvated after being heated. The dried and ground material was heated at 190°C for 16 hours (5 x greater than the longest lifetime in the above desolvation experiment), then cooled to 25°C and left for one hour to allow for resolvation from wet atmospheric air. This cycle was repeated twice, and the sample mass monitored in both cases.

Figure 25 displays the resulting TGA curve. After cooling there was an increase in mass by approximately 2%. This implies that the material has been partially resolvated by atmospheric water. After the second heating phase, on cooling, again a mass increase of about 2% was seen. The results are very interesting as they suggest that AN64 can reversibly adsorb and desorb atmospheric water.

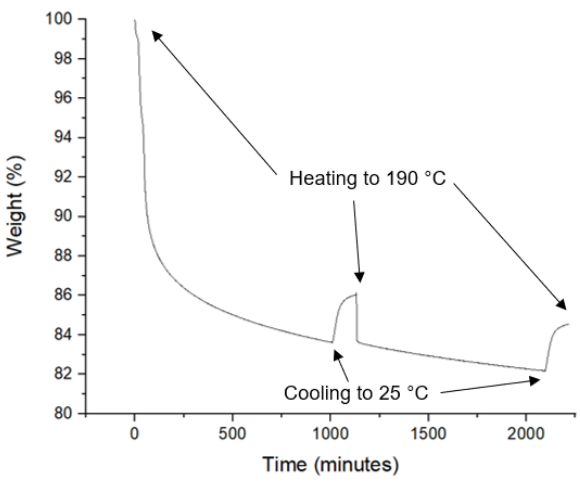

Figure 25: The TGA curve for AN64 during the heating-cooling cycles described in the main text.

In summary, AN64 was found to be mechanically and thermally stable. The thermal stability of AN64 was studied and the resulting TGA mass loss graph appeared to show two overlapping decay curves which could indicate that two different solvent binding sites are present in AN64. A cycled TGA experiment showed AN64 was able to reversibly adsorb and desorb atmospheric water.

2.4 Environmental stability of NOTT-100 crystallites

Clearly, AN64 is stable to both the adsorption and desorption of water. However, not all MOFs are stable to water and other solvents.[82] This section studies the solvent stability of NOTT-100 crystallites. NOTT-100 is a MOF system formed from tetracarboxylate ligands and a copper hydrate salt. NOTT-100 is a well-studied MOF that contains binuclear Cu(II) paddlewheel nodes each bridged by four carboxylate centres.[83]

This section of the thesis, introduction section 1.3 and part of the conclusion have been reproduced from a manuscript that has been prepared for submission. Louisa Davies and Alexander Tansell synthesised the first batch of NOTT-100 crystals and took the SEM images of the NOTT-100 crystallites. Joshua Morris began the process of using ImageJ software to analyse the size of the NOTT-100 crystallites in the SEM

images. I developed the method for extracting particle size distribution from both optical and SEM images using ImageJ software, as well as using Origin to fit the data and to plot the solvent parameter data. I also synthesised the second batch of NOTT-100 crystals and imaged them using an optical microscope.

As discussed in section 1.3, SEM is a very common technique used to visualise MOFs.[39–41] However, there is currently no standardised approach in the field to quantitively assess particle size distribution from such images, despite many articles using SEM to study MOFs.[42] SEM can be used to determine the size of MOF crystals, for example, Xiao-Feng *et al* used SEM to quantify the size of MOF crystals when comparing the size of a MOF crystal and its performance as fluorescence sensor, it was found that different crystal sizes lead to differencing level of performance as a fluorescence sensor.[84]

SEM is a very common technique used to visualise MOFs.[39–41] Over 100,000 articles using SEM to study MOFs have been published.[42] SEM scans a sample with a focussed beam of electrons. The resulting image derived from the electron-sample interactions reveals information about the sample including morphology and particles size, although these are often reported qualitatively. There is no standardised approach in the field to quantitively assess particle size distribution from such images, although issues around voltage selection and sample counting are well discussed in literature.[29] Other similar techniques such as transmission electron microscopy (TEM) have been used to image MOFs.[43] However, the electron beam used in TEM can damage the MOF sample, resulting in a degradation of the framework structure.[44] Dynamic light scattering (DLS) is another primary method used to measure particle size distribution. DLS has the advantage of observing many particles at once, but DLS is typically limited by factors such as the optical configuration of the instrument, laser wavelength and detector sensitivity.[45]

As-synthesised NOTT-100 was first washed with dimethylformamide (DMF) to remove reaction solvents and the crystallites were then washed with a secondary exchange solvent to remove DMF. The synthesis of NOTT-100 is outlined in Figure 26.

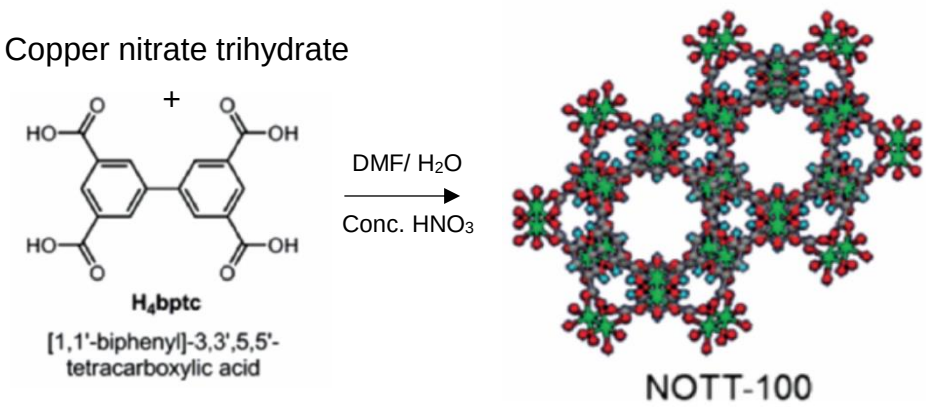

Figure 26: The synthesis of NOTT-100 (images reproduced from Stavila *et al*.).[85]

We were interested in the solvent stability of the crystallites and we therefore imaged the resulting particles by SEM. Four examples of images we obtained are shown in Figure 27.

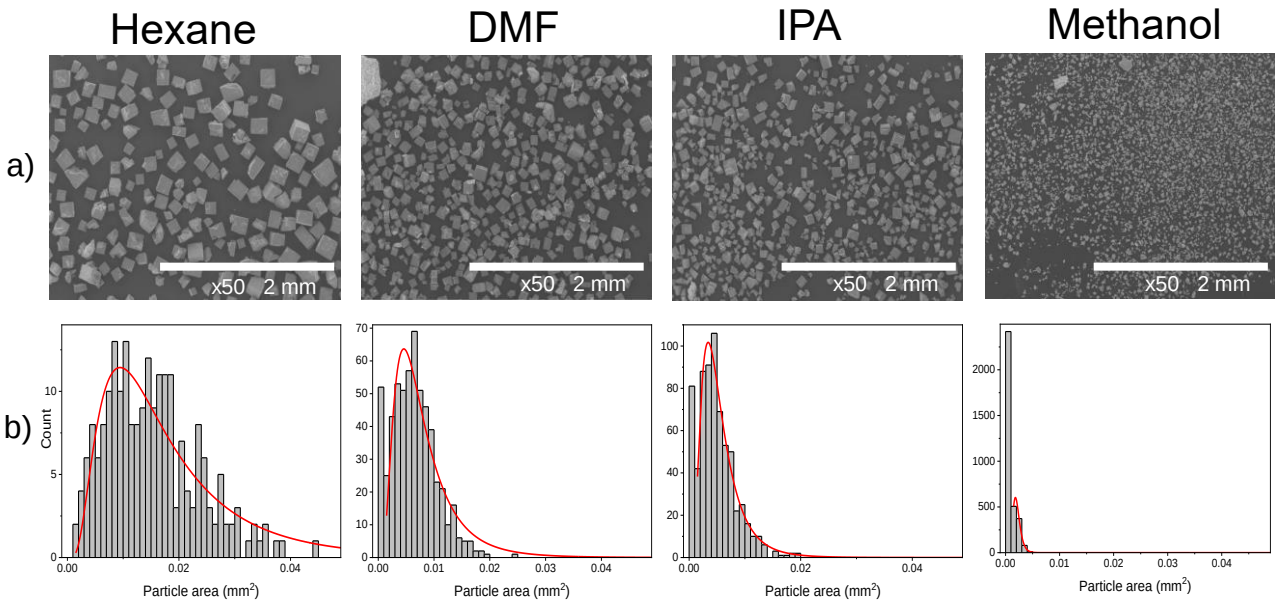

Figure 27: a) SEM images of the NOTT-100 crystals after being washed with a secondary exchange solvent. b) Particle size distribution histograms for four secondary exchanged solvents overlaid with a lognormal fit (red lines).

It was immediately obvious that there is a notable difference in the size distribution of the crystals depending on which secondary exchange solvent was used for washing the crystals. We decided to investigate further and therefore use a range of 12 different solvents (acetone, acetonitrile, chloroform, dichloromethane, dimethylformamide, diethyl ether, ethanol, ethyl acetate, hexane, isopropyl alcohol and methanol). These

solvents were chosen as they are all common laboratory solvents and they had a range of different properties including varied polarity, boiling point and surface tensions. The latter two of these properties are widely implicated in framework collapse during activation before gas sorption experiments.[29] We hypothesised that the observed crystal breakdown in Figure 27 may be a related phenomenon since the first step in SEM experiments is to put the sample under vacuum.

In order to quantitively assess the particle size distributions in the SEM images we developed an image processing protocol described in the SI. The resulting particle size distribution histograms are shown in Figure 27 and for all solvents in Figure 28. In most cases a good fit to the data could be obtained using a lognormal curve (the first bar is ignored in this fit, see SI for details). The distribution centres and widths are shown against solvent parameters in Table 1.

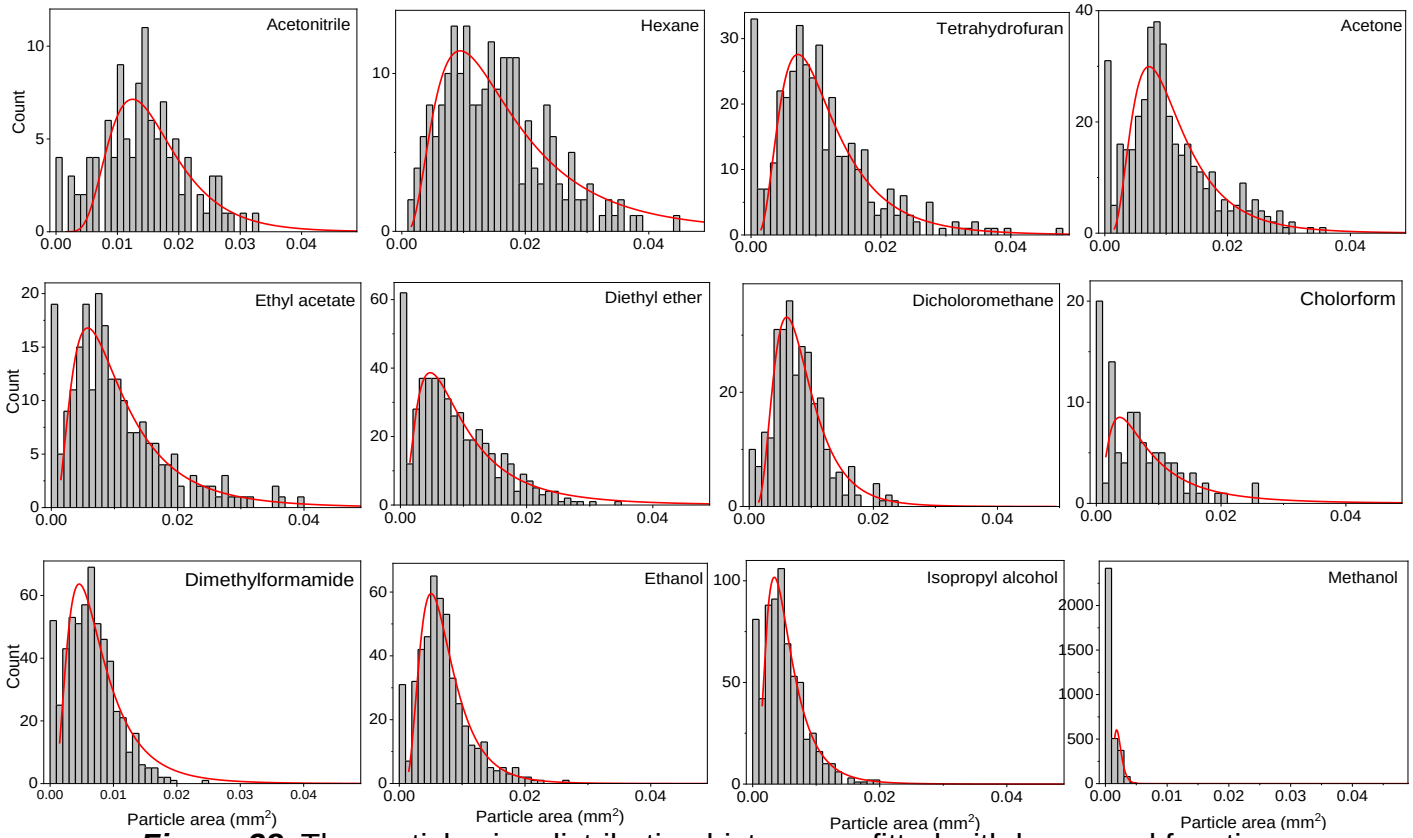

Figure 28: The particle size distribution histograms fitted with lognormal functions (red lines) for each of the NOTT-100 crystallite SEM samples for the twelve different secondary exchange solvent.

Table 1: Solvent properties and the resulting size distribution parameters of the NOTT-100 crystallites after washing with a secondary solvent, as measured by SEM.

	Solvent Parameters								Size Distribution of NOTT-100 crystallites	
Secondary Exchange Solvent	Solvent Donicities from Sandstrom[86]	Solvent Donicities Gutmann revision[87]	Solvent acceptor number[87]	Relative polarity[88]	Boiling point (°C)[89]	Vapour pressure 20 °C (hPa)[89]	Surface tension at 20 °C (mN/m)[89]	Molar volume (cm^3 mol^{-1})	Peak centre x_c ± error (mm^2)	Width of the curve ± error w (mm^2)
Acetone	15	17	12.5	0.355	56.2	240	25.2	74	0.00993 ± 3.84E-04	5.67E-01 ± 0.03
Chloroform	6	4	23.1	0.259	61.2	210	27.5	80.7	0.00733 ± 7.60E-04	0.81907 ± 0.08
DCM	5	1	20.4	0.309	39.8	475	26.5	63.9	0.00774 ± 1.98E-04	0.49955 ± 0.02
DMF	24	26.6	15.5	0.386	153	3.5	37.1	16.0	0.00677 ± 2.060E-04	0.6239 ± 0.02
Diethyl ether	12	19.2	3.9	0.117	34.6	587	16.96	104.8	0.00844 ± 2.09E-04	0.76049 ± 0.02
Ethyl acetate	14	17.1	9.3	0.228	77	97	23.9	9.3	0.00931 ± 3.47E-04	0.6933 ± 0.03
Ethanol	19	19.2	37.1	0.654	78.5	59	22.1	58.5	0.0066 ± 1.31E-04	0.51449 ± 0.02
Hexane	0	0	0	0.009	69	160	18.43	131.6	0.01491 ± 7.91E-04	0.67496 ± 0.04
IPA	18	21.1	33.5	0.546	82.4	44	23	76.8	0.00483 ± 8.16E-04	0.58826 ± 0.01
Acetonitrile	12	14.1	19.3	0.461	81.6	97	29.1	52.6	0.01492 ± 6.62E-04	0.42481 ± 0.04
Methanol	18	19	41.3	0.762	64.6	128	22.7	40.7	0.00202 ± 3.86E-04	0.3245 ± 4.33E-4
THF	17	20	8	0.207	66	200	26.4	81.7	0.01013 ± E-04	0.58115 ± 0.03

In all cases changing the secondary exchange solvent lead to a change in the size distribution of the NOTT-100 crystals as observed by SEM. Interestingly, the morphology of the crystals remained unchanged (small cubes) apart from when methanol was used as the secondary exchange solvent (much smaller particulates were observed). At this stage we were unsure if it was the vacuum applied during SEM or simply a solvent exchange effect that was altering the size of the crystals. To examine the latter option, a new batch of NOTT-100 crystals was synthesised, washed with the twelve secondary exchange solvents and allowed to air dry for 24 hours. The

particles were then imaged using an optical microscope. The particles were notably bigger than in the first batch when first synthesised and there was no clear trend from this second batch in particle size distribution (Figure 29) across the solvent screen. This therefore implicates the SEM process itself in the initially observed changing particle size.

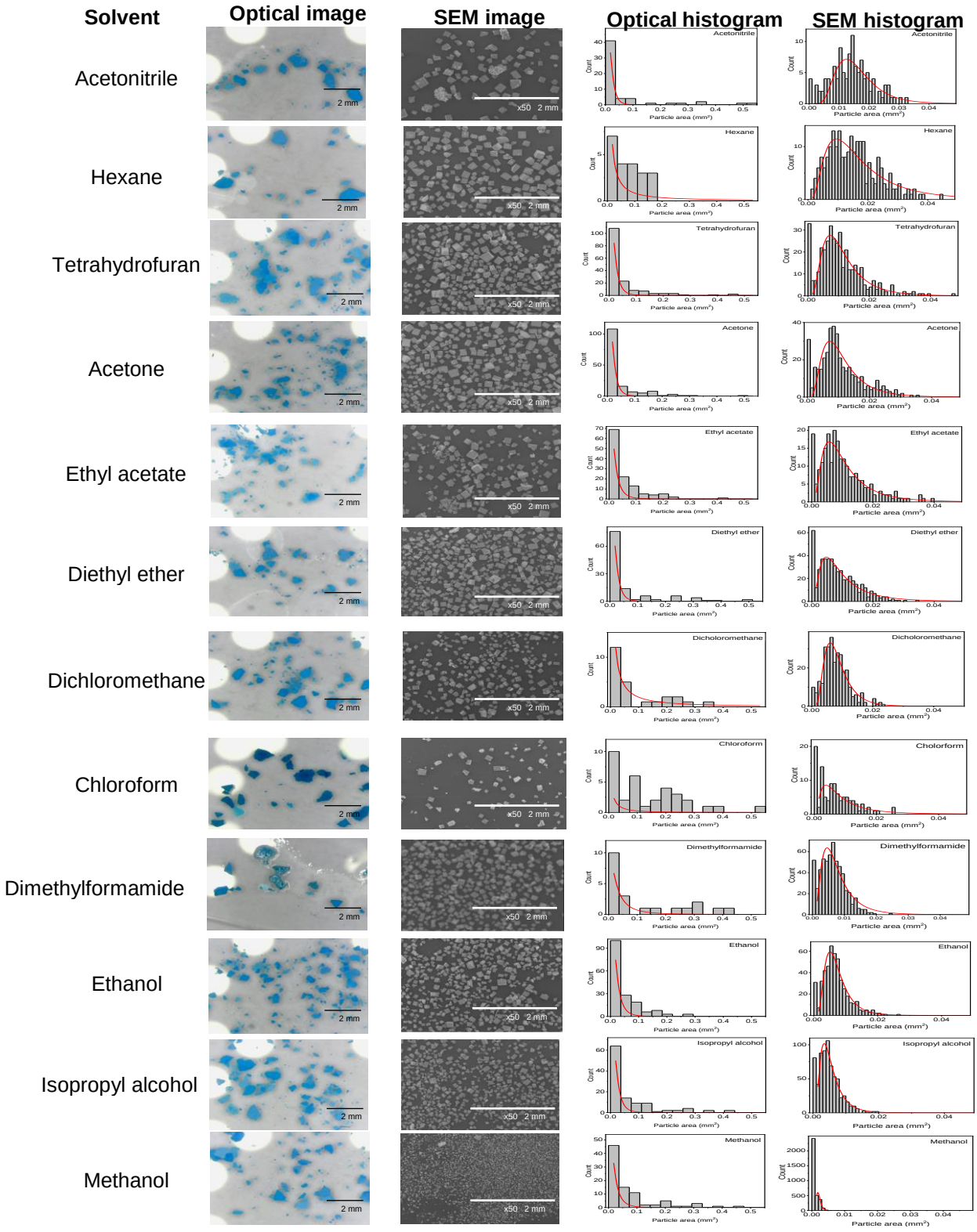

Figure 29: Optical images and SEM images of the NOTT-100 crystals after being washed with a secondary exchange solvent and the resulting particles size distribution histograms for the twelve secondary exchanged solvents overlaid with a lognormal fit (red lines).

The vacuum applied during SEM imaging of the NOTT-100 crystals is the most likely cause of crystal breakdown. During SEM imaging the pressure drops to 10^{-6} Pa in the sample chamber over 2.5 minutes. The resulting rapid evacuation of residual solvent may be the cause of crystal breakdown.

To consider the change in size distribution against differing solvent parameters, such as polarity and solvent acceptor number, these parameters for the secondary exchange solvents were plotted against both the histogram fitted peak centres (x_c) and widths (w) for the twelve SEM measured samples.

For four of the solvent parameters (solvent donor number Gutmann revision, surface tension, vapour pressure and boiling point) no strong correlation was observed with the particle size distribution (Appendix 3). Better correlations were observed for relative polarity, solvent acceptor number, solvent donor number (Sandstrom) and molecular volume, as shown in Figure 30.

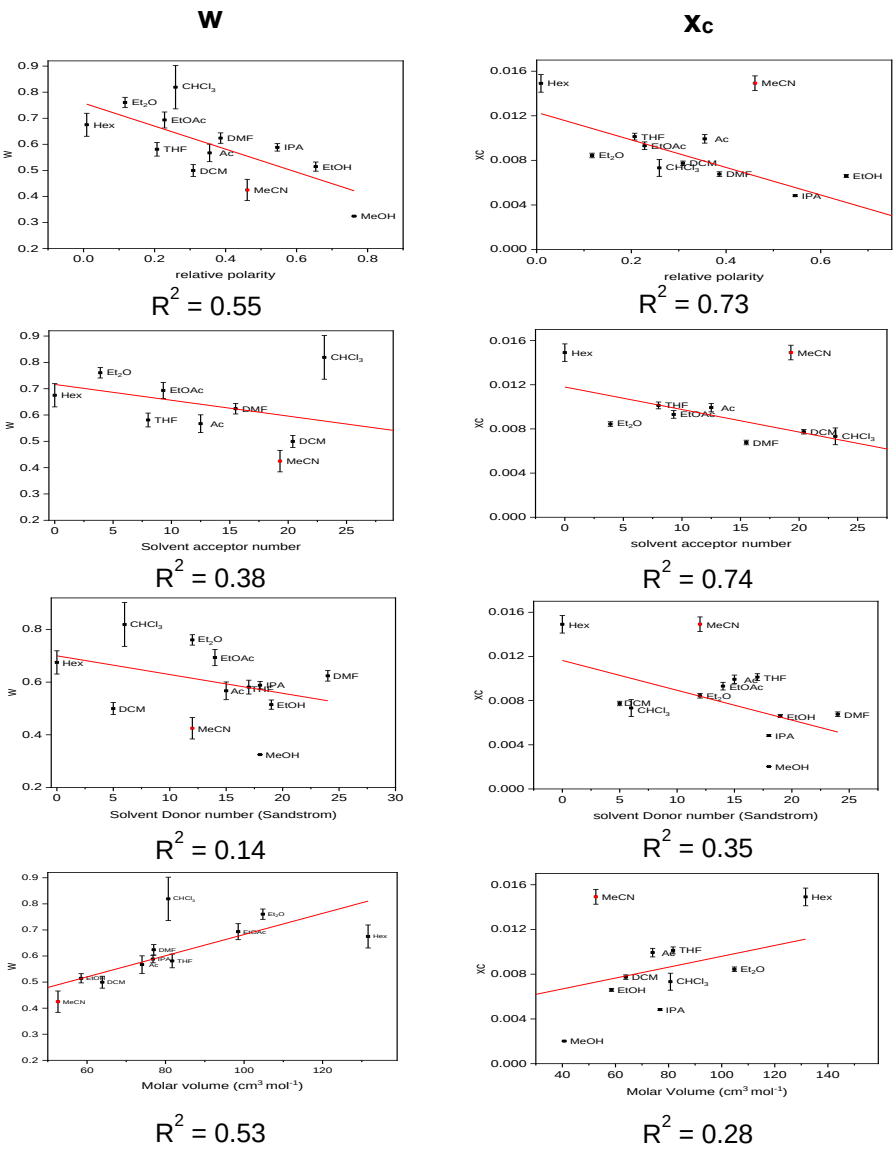

Figure 30: Plots of the particle size distribution histograms curve centre (x_c) for the secondary exchange solvents and width (w) against the different solvent parameters that had a correlation with a linear fit (red line) and accompanying R^2 values. Please note the graphs for the rest of the solvent parameters can be found in Appendix 5.

A linear fit was applied and a correlation between increase in polarity and an associated decrease in w and x_c was observed, R^2 = 0.55 (w) and 0.73 (x_c). A correlation between solvent acceptor number and x_c was observed, however only a weak correlation between solvent acceptor number and w was observed, R^2 = 0.38 (w) and 0.74 (x_c). A weak correlation between solvent donor number (Sandstrom) and w and x_c were observed, R^2 = 0.14 (w) and 0.35 (x_c). Finally, another weak correlation between molecular volume and w and x_c were observed, R^2 = 0.53 (w) and 0.28 (x_c).

While framework collapse on the molecular level is often discussed in terms of solvent surface tension,[29] in our measurements there is no correlation between surface tension and resulting particle size distribution. None of the discussed correlations are

strong enough to be predictive at this stage and we do not know if this phenomenon of SEM damaging the MOF crystals is more general, or if it just afflicts the NOTT-100 MOF studied here, but, the use of vacuum in SEM when imaging MOFs might afflict other MOF systems as well.

Acetonitrile was excluded from the linear fits, it appears to be on outlier in the majority of plots for Figure 30 and in Appendix 3 for reasons still under investigation.

3. Conclusions

A spiropyran core (**SP**) and two photo-active linkers were synthesised (**L1** and **L2**). MOF synthesis was attempted using a combinatorial approach.

Initial combinatorial experiments to form new zirconium-based MOFs involved **L1** and altering the amount and type of modulator used. Crystalline material was observed via PXRD. The PXRD patterns for these crystalline materials exhibited a high intensity peak at approximately 8.5° 2θ. This equates to a d-spacing of *ca*. 10.5 Å, but no vials contained crystals large enough for single crystal X-ray diffraction. In an attempt to grow larger crystals combinatorial experiments were performed at lower temperatures, but this did not lead to larger crystals.

After not forming crystals of suitable quality using **L1**, the extended linker **L2,** was trialled in a series of combinatorial reactions. PXRD showed an intense peak at 8.5° 2θ; a similar peak was observed when the non-extended **L1** was used implying that the linker was not being incorporated into this zirconium-based material. A series of combinatorial control reactions were performed and confirmed that our linker was not being incorporated into this zirconium-based material.

After altering both the modulator and temperature the solvent was changed. DEF was used instead of DMF in a series of reactions with **L1**. After heating for 10 days crystalline material had formed and PXRD showed an intense peak at 13.7° 2θ which equates to a d-spacing of 6.5 Å. Notably the previously observed peak at 8.5° 2θ was not observed in any of these products, suggesting that in the previous experiments, DMF is critical to the formation of that unknown crystalline product.

After the lack of success forming a MOF using zirconium, different metal salts (aluminium nitrate nonahydrate, gallium (III) nitrate hydrate and gadolinium (III) nitrate hexahydrate) were used in combinatorial synthesis with **L1**. After heating none of the aluminium containing vials formed solid. However, when gallium and gadolinium were present amorphous solid formed in each vial. No crystalline products were obtained.

Finally, the amorphous material AN64 was synthesised. The material was found to be unchanged by both grinding with a mortar and pestle, and drying, as confirmed by PXRD. The thermal stability of AN64 was studied using TGA. Interestingly, the resulting TGA mass loss graph appeared to show two overlapping decay curves when the sample was held at 190°C. One has a lifetime of 13 minutes and the other 206 minutes. This could indicate that two different solvent binding sites are present in AN64. We wanted to test if AN64 could be resolvated after being heated. A cycled TGA experiment was performed. At 190°C a mass loss was observed as AN64 was desolvated. Upon cooling, AN64 saw an increase in mass by approximately 2%, which could be repeated. This suggests that AN64 can reversibly adsorb and desorb atmospheric water. “The use of MOFs in water treatment membranes is still in its infancy when compared with its applications for gas separation”[90] however, many MOFs application in liquid separation are limited due to its their low stability in water caused by the interaction of coordinatively unsaturated metal sites with the water molecules.[91] The fact that AN64 appears to be stable and can reversibly adsorb and desorb atmospheric water makes it an exciting material for having potential desalination ability.

The second part of this thesis studied the size and stability of NOTT-100 crystallites. In this study, clearly the SEM measurement itself is not innocent. The more polar and higher acceptor number solvents, even when only present in residual amounts after air drying, are enough to break up the crystallites when they are exposed to vacuum. There was no apparent trend between the secondary exchange solvent and the particle size distribution in the optical images of the crystals, prior to the SEM measurement. There is a correlation between increasing polarity of the secondary exchange solvent and a decrease in the x_c and w values in the SEM experiments. There is also a correlation between increasing solvent acceptor number for the secondary exchange solvent and a decrease in the Xc and W values. None of these correlations are strong enough to be predictive at this stage and we do not know if this phenomenon of SEM damaging the MOF crystals is more general, or if it just afflicts the NOTT-100 MOF studied here – no other literature reports currently exist on this phenomenon. However, seeing as the size of MOF crystallites can affect the performance of MOFs,[84] it is certainly worth noting the findings of this initial result, as other MOF systems may be afflicted by this phenomenon of SEM damaging the MOF

crystals. Moreover, seeing as SEM is a very common technique used to visualise MOFs,[42] and as there is currently no standardised approach in the field to quantitively assess particle size distribution from such images it is worth considering if there should be a standard approach to assess the size distribution of MOF particle size distribution.

4. Future work

Initially it would be worth performing UV-Vis studies on **L2** in solution in order to better characterise the photo-physics of the molecule. Previous students in the Easun group have studied the UV-vis absorption and emission properties of **L1**, but these studies are yet to be done on **L2**. It is also worth performing more MOF combinatorial synthesis with **L2**.

After the lack of success forming crystalline material by altering the amount of modulator whilst keeping the ratios of linker and zirconium salt the same, it is worth considering altering these ratios.

Another logical next step is to continue performing combinatorial synthesis with Ga and Gd. The next sets of combinatorial experiments could involve using different solvents such as DEF or using other modulators that have not been tried with these metals such as L-proline or benzoic acid.

The continued characterisation of AN64 is an important next step. Variable temperature PXRD would show how altering the temperature alters the powder pattern of the material. Once the PDF data is received from our collaborator it will be interesting to see if this data can tell us about the local structure of this amorphous material at the atomic scale.

The second part of this thesis involved studying the size and stability of NOTT-100 crystallites. A logical next step would be to consider studying different MOFs. For instance, it would be interesting to study a MOF with the same tetracarboxylate linker as NOTT-100, but with a different metal, such as MFM-300(Ga_2).[92]

It is also worth performing computational modelling of framework mechanical stability of this phenomenon. Computational modelling may give us a greater understanding of how the SEM vacuum and trace amounts of residual solvent are causing the breakdown of the NOTT-100 crystallites.

5. Experimental

5.1 General information

All chemical reagents and solvents were bought from commercial suppliers without the need of any further purification. All compounds synthesised in the Experimental procedure have been characterised using a minimum of ^{1}H nuclear magnetic resonance and low-resolution mass spectrometry. Promising results from the combinatorial syntheses were analysed using powder X-ray diffraction by wet-loading the samples on zero-background silicon wafers.

^{1}H Nuclear Magnetic Resonance (NMR)

All samples were analysed using a 400 MHz frequency on a Bruker 400 Ultrashield™.

Low-resolution Mass Spectrometry (LRMS)

A Waters LCT Premier XE spectrometer was used to obtain all LRMS data.

Fourier-transform Infrared Spectroscopy (FT-IR)

IR data was obtained using a SHIMADZU IRAffinitt-1S fitted with an ATR attachment.

Powder X-ray Diffraction (PXRD)

An X'Pert PRO PANalytical Chiller 59 with an X'Celerato laser was used to obtain all powder XRD data with the copper K_{α} wavelength of radiation (1.5406 Å). The scan range was between the values of 4 and 40 for 2θ with each scan lasting 30 minutes.

Thermogravimetric analysis (TGA)

A PerkinElmer Pyris 1 TGA was used to obtain all of the TGA data. under a flow of air (20 mL/min) using a heating rate of 5 °C/min.

Optical images

Optical images for the NOTT-100 crystals were recorded using a Jiusion 40 to 1000x Magnification Endoscope, 8 LED USB 2.0 Digital Microscope.

Optical images for section 2.2 (Figure 18) were recorded using a Motic SMZ-161 with polarizer accessory microscope.

SEM images

Scanning Electron Microscopy images were collected using a HITACHI TM3030Plus Table top Microscope. Samples collected using a HITACHI TM3030Plus Tabletop Microscope were prepared on adhesive tape.

5.2 Experimental procedure for part 1

Synthetic procedures for the mono-brominated spiropyran, di-brominated spiropyran (**SP**), isophthalate boronic acid, protected-isophthalate boronic acid,
protected non-extended isophthalate spiropyran and the deprotected non-extended isophthalate spiropyran linker (**L1**) were taken from the thesis of Dr Magdalene Chong.[93]

Synthetic procedures for the DAN-protected boronic acid, protected para-carboxylate boronic acid, DAN-protected ester-protected boronic acid, ester-protected extended boronic acid, ester-protected extended spiropyran linker and the extended spiropyran linker (**L2**) were taken from the thesis and preliminary PDRA work of Dr Adam Nevin.[94] Please note for all bromine containing species the LRMS(EI) found m/z and calculated m/z may bye slightly different due to the present of bromine isotope peaks.

Mono-brominated spiropyran

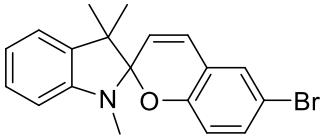

1,3,3 trimethyl-2-methyleneindoline (4.5 ml, 24.8 mmol) was added to a stirred solution of 5-bromosalicylaldehyde (5.00 g, 24.8 mmol) in ethanol (75 mL). The pink solution was heated to reflux for 24 hours at 80°C. After cooling to room temperature, the flask was placed in the freezer for 4 hours. The contents of the flask were filtered, the solid was washed with ethanol and then dried in a desiccator overnight to yield a pale pink solid. Yield: 5.78 g, 66 %. **^{1}H NMR** (400 MHz, $CDCl_3$): δ ppm = 1.18 (s, 3H), 1.31 (s, 3H), 2.74 (s, 3H), 5.75 (d, J = 10 Hz, 1H), 6.55 (d, J = 8 Hz, 1H), 6.62 (d, J = 9 Hz, 1H), 6.80 (d, J = 10 Hz, 1H), 6.87 (t, J = 7 Hz, 1H), 7.10 (d, J = 7 Hz, 1H), 7.19 (m, 3H). **LRMS(EI)** found m/z = 355.04; calculated m/z = 356.26 for $C_{19}H_{18}BrNO$.

Di-brominated spiropyran (SP)

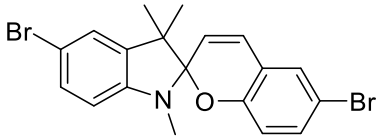

Mono-brominated spiropyran (2.89 g, 8.11 mmol) and N-bromosuccinimide (1.44 g, 8.11 mmol) were dissolved in chloroform (160 mL). The mixture was left to stir at room temperature for 5 days. After 5 days the mixture was heated to reflux for 1 hour. The flask was then cooled to room temperature and its contents filtered and washed with chloroform, then extracted with water (3 x 100 mL) and dried over magnesium sulphate. Solvent was removed under reduced pressure to yield a green oil which was recrystallised using hot ethanol to yield a cream solid. Yield: 1.69 g, 48 %. **^{1}H NMR** (400 MHz, $CDCl_3$): δ ppm = 1.08 (s, 3H), 1.19 (s, 3H), 2.71 (s, 3H), 5.61 (d, J = 10 Hz, 1H), 6.31 (1H, d, J = 8 Hz, CH), 6.53 (m, 1H), 6.72 (d, J = 10 Hz, 1H), 7.14 (d, J = 2 Hz, 1H), 7.19 (dd, J = 8 Hz, 1H). **LRMS(ES)** found m/z = 435.97; calculated m/z = 435.16 for $C_{19}H_{17}Br_2NO$.

Isophthalate boronic acid

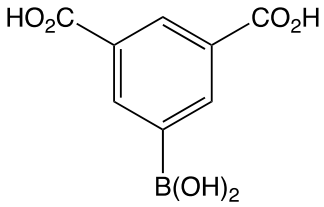

3,5-dimethylboronic acid (5.01 g, 33.4 mmol) and sodium hydroxide (4.75 g, 0.12 mol) were dissolved in water/tert-butanol (v/v = 3:1, 160 mL) and the solution was heated to 60°C. Potassium permanganate (ca. 25 g) was added in small aliquots over 1 hour. The mixture was heated to 70°C and additional potassium permanganate (ca. 15 g) added. The mixture was stirred for 24 hours. Isopropanol (25 mL) was added to the mixture and was left to stir for 3 days at room temperature. The reaction was filtered while hot and the filtrate reduced under vacuum to 30 mL which left a clear solution. The solution was acidified with hydrochloric acid (12 M) to form a white precipitate which was filtered, washed with water and dried to yield a white solid. Yield: 4.30 g, 61%. **^{1}H NMR** (400 MHz, $(CD_3)_2SO$)): δ ppm = 8.58 (s, 2H), 8.72 (s, 1H). **LRMS(ES)** found m/z = 209.00; calculated m/z = 209.95 for $C_8H_7BO_6$.

Protected-isophthalate boronic acid

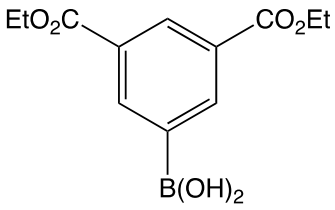

To a stirred solution of isophthalate boronic acid (4.30 g, 20.5 mmol) in ethanol (200 mL), sulfuric acid (12 M, 5 mL) was added and left to reflux for 1 day at 80°C. After cooling to room temperature, the solvent was reduced under vacuum to ca. 30 mL. Water was added until precipitation. This was filtered and washed was copious amounts of water (ca. 1 L) until the filtrate was neutral (pH 7). The solid was dried overnight to yield a white solid. Yield: 3.53 g, 65%. **^{1}H NMR** (400 MHz, $(CD_3)_2SO$): δ_H = 1.36 (t, J = 6 Hz, 6H), 4.37 (m, 4H), 8.51 (s, 1H), 8.64 (s, 2H). **LRMS(ES)** found m/z = 267.09; calculated m/z = 265.96 for $C_{12}H_{15}BO_6$.

Protected non-extended isophthalate spiropyran

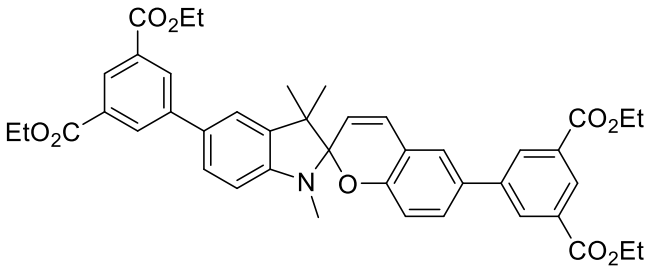

To a degassed stirring solution of **SP** (1.10 g, 25.2 mmol), 5-borono-1,3-benenzedicarboxylic acid (1.86 g, 69.9 mmol) and potassium carbonate (0.73 g) in toluene/water (v/v = 4:1, 85 mL), tris(dibenzylideneacetone)dipalladium(0) (0.24 g**,** 0.26 mmol) and tri-tert-butylphosphine (0.4 mL, 1.65 mmol) were added and the reaction vessel left for 24 hours at 80°C. The contents were filtered whilst hot through a 1 cm silica plug. The filtrate washed with water and dichloromethane (v/v = 1:1, 3 x 200 mL). The organic layer was extracted and dried over magnesium sulphate and the remaining solvent was removed under reduced pressure to yield a brown oil. The oil was recrystallised from dichloromethane/methanol to yield a yellow solid. Yield 1.08 g, 60 %. **^{1}H NMR** (300 MHz, $(CD_3)_2SO$): δ ppm = 1.27 (s, 3H), 1.32 (t, J = 8 Hz, 6H), 1.90 (s, 3H), 2.71 (s, 3H), 4.31 (q, J = 9 Hz, 4H), 5.64 (d, J = 12 Hz, 1H), 6.65 (d, J = 4 Hz, 1H), 6.87 (d, J = 12 Hz, 1H), 7.05 (d, J = 8 Hz, 1H), 7.40 (s, 2H), 7.44 (dd, J = 12 Hz, 1H), 7.52 (m, 1H), 8.41 (s, 2H), 8.49 (d, J = 8 Hz, 2H), 8.59 (s, 1H), 8.62 (s, 1H). **LRMS(ES)** found m/z = 718.30; calculated m/z = 717.82 for $C_{43}H_{43}NO_9$.

Deprotected non-extended isophthalate spiropyran linker (L1)

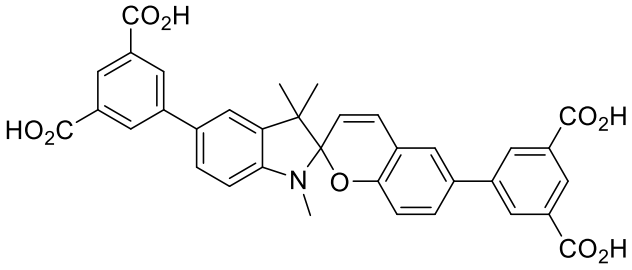

To a stirring solution of the protected non-extended isophthalate spiropyran (1.01 g, 1.40 mmol) in anhydrous tetrahydrofuran (100 mL) potassium trimethylsilanolate (1.01 g, 7.80 mmol) was added and the reaction was left to stir at room temperature for 3 days. The remaining solvent was removed under reduced pressure to yield a yellow solid. The solid was dissolved in boiling water and was then acidified to pH 1 using hydrochloric acid (12 M). The resulting red solid was filtered and dried to yield a black solid. Yield: 0.70 g, 83 %. **^{1}H NMR** (400 MHz, $(CD_3)_2SO$): δ ppm = 1.15 (s, 3H), 1.30 (s, 3H), 2.70 (s, 3H), 5.85 (d, J = 4 Hz, 1H), 6.69 (d, J = 8 Hz, 1H), 6.77 (d, J = 8 Hz, 1H), 7.14 (d, J = 10 Hz, 1H), 7.47 (m, 3H), 7.62 (d, J = 3 Hz, 1H), 8.36 (t, J = 11 Hz, 1H), 8.39 (m, 5H), **LRMS(ES)** found m/z = 606.18; calculated m/z = 605.60 for $C_{35}H_{27}NO_9$. **FT-IR**: ν_{max} (cm^{-1}) = 1709, 1591, 1535, 1371, 1306, 1233, 1105, 1069, 1022, 999, 959, 812, 756, 714, 669, 642.

DAN-protected boronic acid

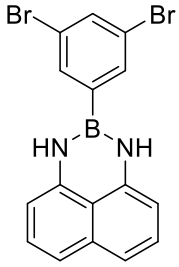

3,5-dibromophenylboronic acid (10.02 g, 35.9 mmol) was dissolved in toluene (170 mL). 1,8-diaminonaphthalene (DAN) (6.60 g, 35.9 mmol) was added to the solution to form a brown solution, which was left to stir for 1 hour at 100°C. Once cooled, the solvent was removed under reduced pressure to yield a brown solid which was dissolved in the minimum amount of boiling dichloromethane (ca. 500 mL) whilst stirring at 40°C. Petroleum ether was added until precipitation. The resulting suspension was cooled, filtered and then washed with petroleum ether to yield a pale

green solid. Yield: 9.40 g, 65 %. **^{1}H NMR** (400 MHz, $(CD_3)_2SO$): δ ppm = 6.58 (d, J = 8 Hz, 2H), 6.94 (d, J = 8 Hz, 2H), 7.10 (t, J = 8 Hz, 2H), 7.93 (t, J = 4 Hz, 2H), 8.17 (d, J = 4 Hz, 2H), 8.45 (s, 1H). **LRMS(EI)** found m/z = 401.94; calculated m/z = 401.89 for $C_{16}H_{11}BBr_2N_2$.

Protected para-carboxylate boronic acid

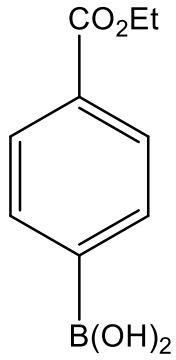

4-carboxyphenylboronic acid (5 g, 30 mmol) was and concentrated sulphuric acid (1.5 ml) were added to ethanol (125 ml).The solution was heated to 85°C for 20 hours. After heating the volume of the solution was reduced under reduced pressure until precipitation occurred. Excess water was added to the resulting suspension and the suspension was filtered. The resulting white product was washed with water until the pH of the filtrate was neutral. Yield = 3.90 g, 67 %. **^{1}H NMR** (400 MHz, $(CD_3)_2SO$):): δ ppm= 1.35 (t, J = 7.0 Hz, 3H), 4.36 (q, J = 7.0 2H), 7.83 (m, 2H), 8.60 (m, 2H, **LRMS(EI)** found m/z = 194.08; calculated m/z = 194.08 for $C_9H_{11}BO_4$

DAN-protected ester-protected boronic acid

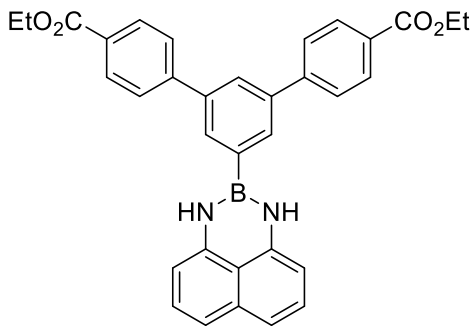

Ester-protected 4-carboxyphenylboronic acid (2.2 g, 10 mmol) and potassium carbonate (0.56 g, 4.05 mmol) were added to a stirring degassed solution of DAN-protected boronic acid (1.91 g, 4.76 mmol) in toluene/water (v/v = 4:1, 250 ml). The solution was heated to 60˚C. Then tri-tert-butyl phosphine (0.30 ml, 1.3 mmol, commercial 1 M solution in toluene) and tris(dibenzylideneacetone)dipalladium(0) (176 mg, 0.19 mmol) were added. The reaction was heated at 80 ˚C under inert atmosphere for 20 hours. The reaction mixture was filtered, washed and extracted with dichloromethane and water (v/v = 1:1, 300 ml). The orange organic layer was dried over magnesium sulphate, filtered and the solvent removed under reduced pressure to yield a brown solid. Yield: 2.01 g, 77 %. **^{1}H NMR** (400 MHz, $CDCl_3$): δ ppm = 1.46 – 1.31 (m, 6H), 4.35 (q, 4H), 6.10 (s, 1H), 6.40 (dd, *J* = 7.3, 0.9 Hz, 2H), 7.00 – 7.15 (m, 5H), 7.36 – 7.41 (m, 1H), 7.67 (s, 1H), 7.70 (s, 1H), 7.80 (d, *J* = 1.8 Hz, 1H), 7.84 (t, *J* = 1.8 Hz, 1H), 8.03 (m, 1H), 8.10 (m, 3H). **LRMS(ES)** found m/z = 541.23; calculated m/z = 541.23 for $C_{34}H_{30}O_4N_2B$.

Ester-protected extended boronic acid

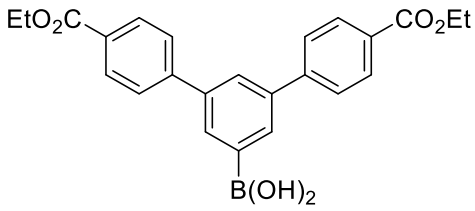

To a stirring solution of the DAN-protected ester-protected boronic acid (0.8 g, 1.48 mmol) in tetrahydrofuran (50 ml), 2M sulphuric acid (10 ml) was added and the brown reaction mixture was stirred at 70˚C for 24 hours. The resulting dark brown mixture was filtered while hot with water and was washed with water until the filtrate was neutral. Yield: 0.5 g, 81 %. ^{1}H NMR (400 MHz, $(CD_3)_2SO$): 1.36 (t, J = 7.1 Hz, 6H), 4.36 (q, 4H), 7.97 (m, 3H), 8.09 (m, 5H), 8.21 (d, J = 1.8 Hz, 1H), 8.37 (s, 2H). **LRMS(ES)** found m/z = 419.17; calculated m/z = 417.16 for $C_{24}H_{22}O_6B$.

Ester-protected extended spiropyran linker

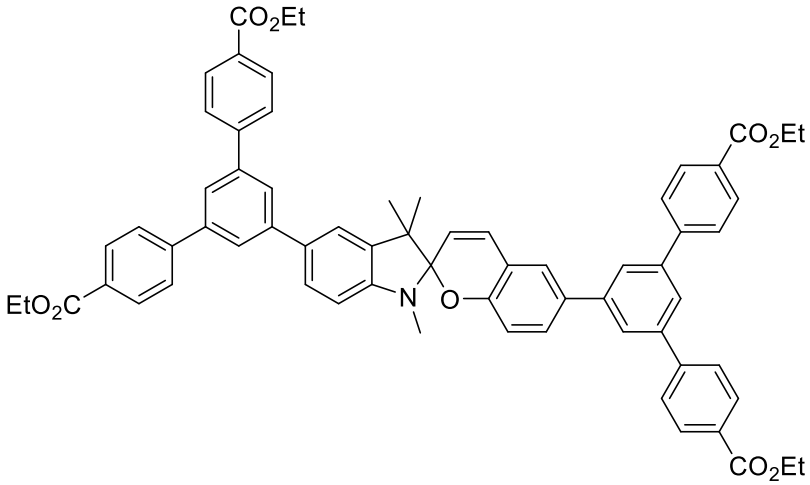

SP (1.36 g, 3.13 mmol), the ester-protected extended boronic acid (3.14 g, 8.04 mmol), and tri-potassium phosphate (3.0 g, 15.14 mmol) were added to toluene/water (v/v = 4:1, 130 ml) at 60 ˚C while stirred under an inert atmosphere. Tricyclohexylphosphine (0.048 g, 0.18 mmol) and tris(dibenzylideneacetone)dipalladium(0) (0.064 g, 0.06 mmol) were added and the temperature of the reaction mixture was raised to 100˚C for 24 hours. The reaction mixture was filtered while hot. The filtrate was washed and extracted with dichloromethane and water (v/v = 1:1, 3 x 100 ml). The organic layer was dried over

magnesium sulphate, filtered and evaporated to dryness to yield a brown oil. The oil was recrystallised from dichloromethane/methanol to yield a yellow solid. Yield: 0.62 g, 19 %. **^{1}H NMR** (400 MHz, $CDCl_3$): δ ppm = 1.26 (s, 6H), 1.44 (t, *J* = 7.0 Hz, 12H), 2.80 (m, 3H), 4.42 (q, *J* = 7.2 Hz, 8H), 5.77 (m, 2H), 6.41 (d, *J* = 8.2 Hz, 1H), 6.66 (dd, *J* = 7.8 Hz, 1H), 6.87 (m, 1H), 6.97 (m, 1H), 7.17 (d, *J* = 2.0 Hz, 1H), 7.40 (dd, *J* = 8.4 Hz, 2H), 7.53 (m, 1H), 7.77 (m, 10H), 7.88 (m, 2H), 8.17 (m, 8H). **LRMS(ES)** found *m/z* = 1022.43; calculated *m/z* = 1022.52 for $C_{67}H_{59}NO_9$.

Extended spiropyran linker (L2)

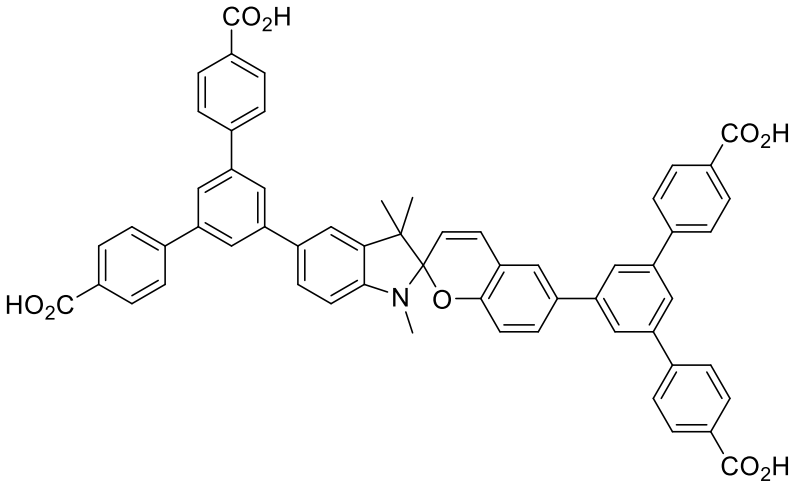

Potassium trimethylsilanolate (0.7 g, 5.4 mmol) was added to a stirred, degassed solution of the ester-protected extended spiropyran linker (0.26 g, 0.26 mmol) in tetrahydrofuran (40 ml). The reaction mixture stirred at room temperature for 24 hours. The solvent was removed under reduced pressure to yield a light brown solid. The solid was dissolved in the minimum volume of boiling water and the stirred solution was acidified to pH 1 using concentrated hydrochloric acid. The black precipitate was filtered and dried. Yield: 147 mg, 63 %. **^{1}H NMR** (400 MHz, $(CD_3)_2SO$): δ ppm = 1.26 (d, *J* = 3.1 Hz, 6H), 2.78 (s, 3H), 5.84 (d, *J* = 10.2 Hz, 1H), 6.57 (d, *J* = 7.7 Hz, 2H), 6.69 (dd, *J* = 8.6 Hz, 1H), 6.84 (m, 1H), 7.17 (m, 4H), 7.26 (m, 1H), 7.29 (m, 2H), 7.67 (m, 7H), 7.80 (m, 6H), 7.97 (m, 7H), 8.12 (m, 3H). **FT-IR**: ν_{max} (cm^{-1}) = 1701, 1601, 1596, 1475, 1396, 1230, 1175, 1051, 1000, 953, 860, 775, 698, 525, 475. **LRMS(ES)** found *m/z* = 910.3; calculated *m/z* = 910.30 for $C_{59}H_{44}NO_9$.

5.3 Experimental procedure for part 2

Synthesis of biphenyl-3,3',5,5'-tetramethyl

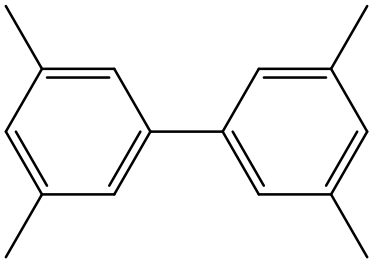

Bromo-*meta*-xylene (4.09 g, 22.1 mmol), 1,3-dimethyl-5-boronic acid (3.25 g, 21.7 mmol), cesium carbonate (7.04 g, 21.7 mmol) and tetrakis(triphenylphosphine)palladium(0) (250 mg) were dissolved in anhydrous ethanol (100 ml) to form an orange mixture. The mixture was heated for 50 hours at 80°C. The resulting mixture was filtered and the solvent was removed under reduced pressure. The resulting orange oil was dissolved in the minimum amount of hexane and was purified using 40-60 µm silica eluted with hexane. The resulting solution had solvent removed under reduced pressure to yield a white solid. Yield = 4.5 g, 99%, **^{1}H NMR** (400 MHz, $CDCl_3$) δ ppm 2.4 (s, 12H), 7.0 (s, 2H), 7.2 (s 4H). **LRMS(ES)** found *m/z* = 211.14; calculated *m/z* = 211.5 for $C_{16}H_{18}$.

Synthesis of biphenyl-3,3',5,5'-tetracarboxylic acid

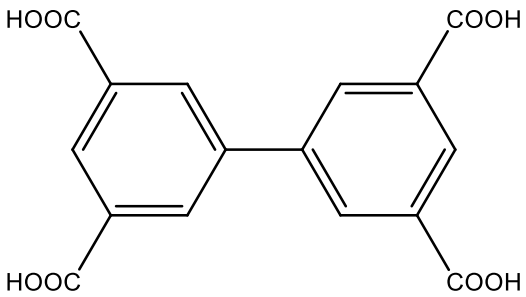

Sodium hydroxide (5 g, 0.15 mmol) was dissolved in water (150 ml) and t-butanol (150 ml). 3',5,5'-tetramethylbiphenyl (4.5g, 0.02 mol) was added to the mixture and was stirred at 50°C for 30 minutes to form a clear solution. Potassium permanganate (65 g) was added over 8 hours until a purple colour persisted in the solution. Heat was increased to 70°C and the mixture was left to stir for 72 hours. Isopropyl alcohol (20 ml) was added to the mixture and stirred for 30 minutes. The mixture was filtered through a sinter with a celite pad. The resulting brown solid was washed with boiling water (3 x 100 ml) and with boiling sodium hydroxide (100 ml, 1M). The filtrate was concentrated to 25 ml and was acidified to pH1 using 12M HCl. The resulting white solid was isolated by vacuum filtration to yield a cream coloured solid. Yield = 5.5 g, 70 %, **^{1}H NMR** (400 MHz, $(CD_3)_2SO$)) δ ppm: 7.0 (s), 8.4 (s, 4H), 8.5 (s, 2H). **LRMS(ES)** found *m/z* = 330.04; calculated *m/z* = 329.10 for $C_{16}H_{10}O_8$.

NOTT-100 combinatorial synthesis

Copper nitrate trihydrate (20.3 mg, 0.084 mmol) and biphenyl-3,3',5,5'-tetracarboxylic acid (13.9 mg, 0.042 mmol) were added to a Wheaton vial with water (1 ml), DMF (2 ml) and concentrated nitric acid (90 µl). The vials were sealed and heated in an aluminium block at 55°C for five days. The reaction mixture was solvent-exchanged with DMF (3x20 ml) and three times with a secondary solvent.

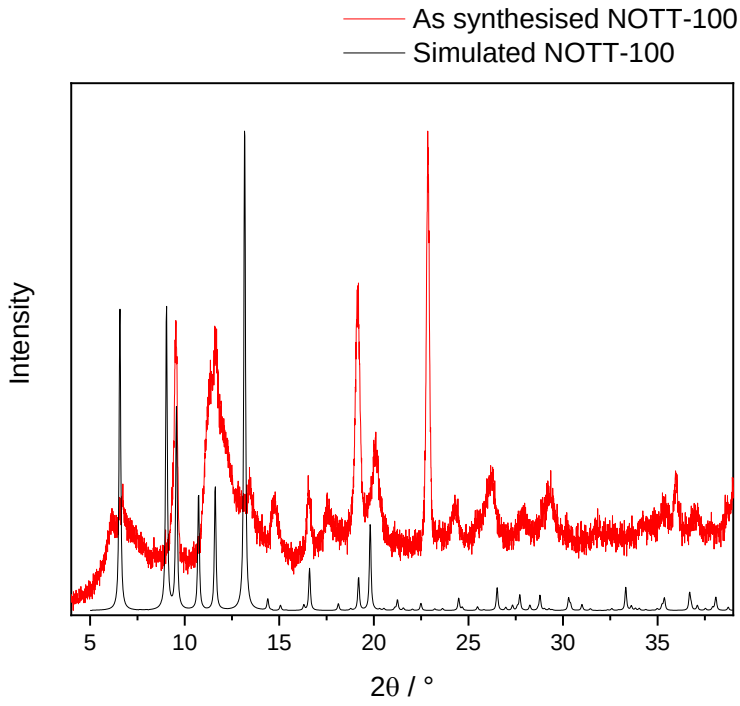

Figure 31: The PXRD pattern of NOTT-100 crystals as synthesised and the simulated NOTT-100 PXRD pattern.

Washing procedure

After the NOTT-100 crystals were solvent exchanged with DMF the resulting blue crystals were equally divided in 12 vials. Each vial was washed three times with a secondary exchange solvent (3x2 ml). 12 different secondary exchange solvents were used (acetone, acetonitrile, chloroform, dichloromethane, dimethylformamide, diethyl ether, ethanol, ethyl acetate, hexane, isopropyl alcohol and methanol).

Image processing

The optical and SEM images of NOTT-100 were imaged using Fiji software which was downloaded from: https://fiji.sc/#download. An 'Adjustable Watershed' plugin was added to the Fiji software. The 'Adjustable Watershed' plugin was downloaded from: http://imagejdocu.tudor.lu/doku.php?id=plugin:segmentation:adjustable_watershed:start

The histograms and curves were fitted and generated in Origin 64-bit.

The images were directly loaded in Fiji. Firstly, the image was converted to an 8-bit image (Figure 32).

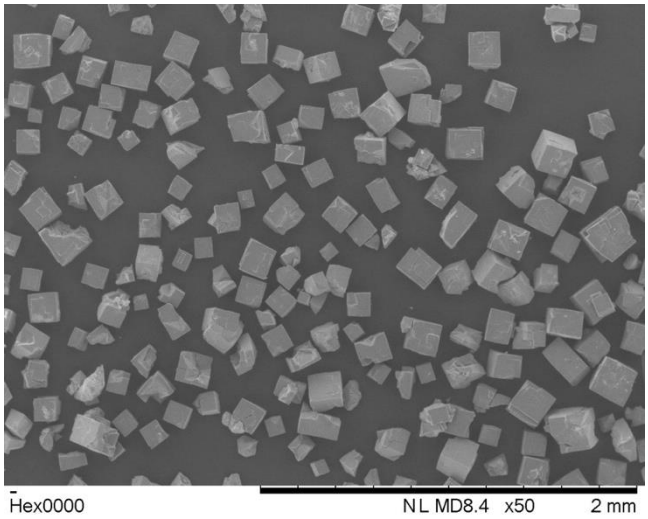

Figure 32: The SEM image of NOTT-100 washed with hexane before image processing.

The image was then subject to a bandpass filter in the imagej software to enhance the contrast between the background and the crystals (Figure 33).

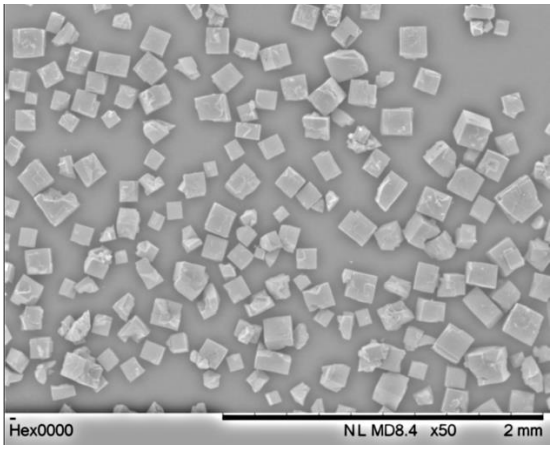

Figure 33 The SEM image of NOTT-100 washed with hexane after a bandpass filter has been applied to the image.

The image was then put through a threshold to remove as much of the background noise and the images as possible without removing any real crystals (Figure 33) and the image was then converted to a binary image to allow the adjustable watershed to be applied (Figure 34).

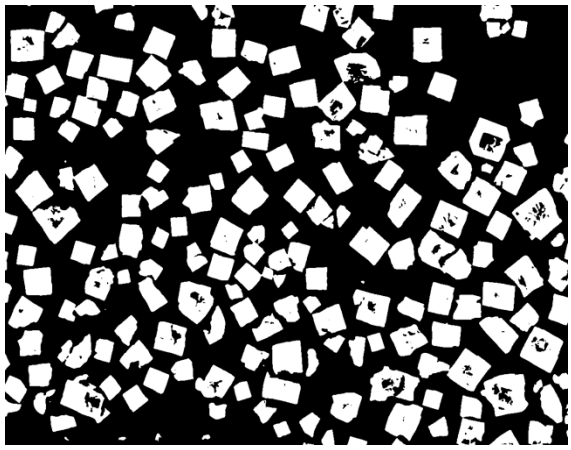

Figure 34: The SEM image of NOTT-100 washed with hexane after being put through the threshold and after being converted to a binary image.

Afterwards the 'Adjustable Watershed' plugin was used to separate any overlapping crystals. The watershed was used to ensure that overlapping crystals were not counted as one larger crystal, but rather as smaller crystals. This tool algorithmically divides composite crystals into individual parts that better represent the individual crystals in any given clump.[95]

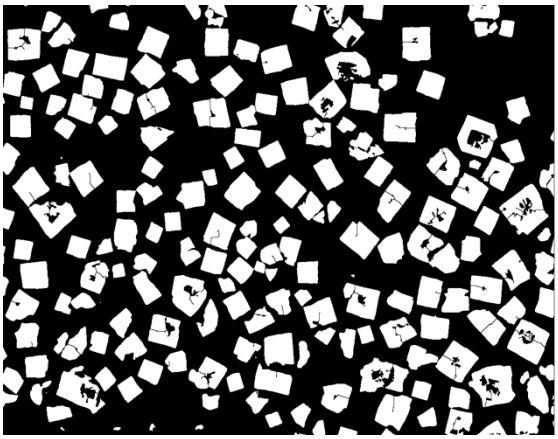

Figure 35: The SEM image of NOTT-100 washed with hexane after the crystals have been separated using the adjustable watershed plugin.

Figure 36 shows the histograms generate from the images in Figure 34 and Figure 35. The histograms show that using the adjustable watershed allows the separation of overlapping crystals whilst having little overall effect on the shape of the histogram.

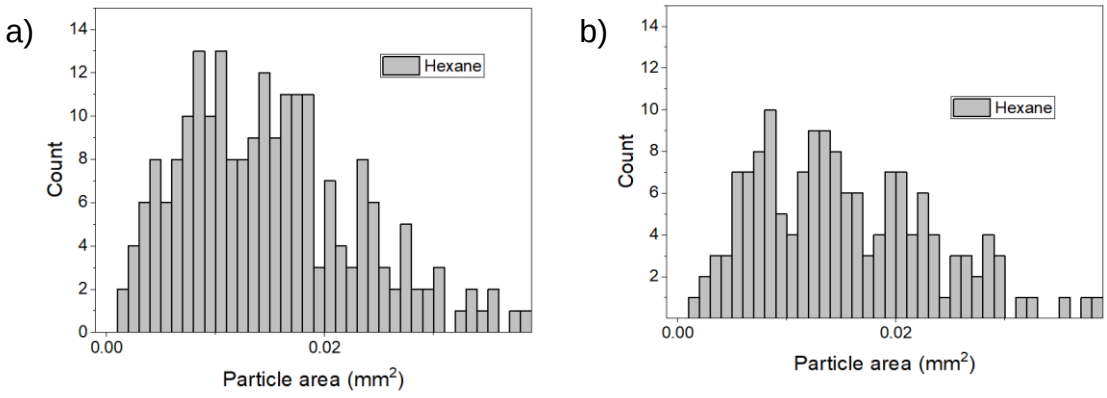

Figure 36: The histogram of particle size distribution of the NOTT-100 crystallites which were secondary-solvent exchanged with hexane with adjustable watershed (a) and without an adjustable watershed (b).

The image was scaled using either the scale bar on the image (for SEM images) or using a S8-stage mic 1 mm/0.01 graticule (for optical images). Finally, the particles were analysed and the sizes of the crystals in mm^2 was recorded. Any particles that were found to be less than 6.36×10^{-5} mm^2 were removed from the analysis. This is the size of a 3 x 3 pixel square, any particles smaller than this were not visible on the image by eye and were deleted.

The particle size data was then transferred to Origin 64-bit. The particle size data was then used to generate a histogram (Figure 37).

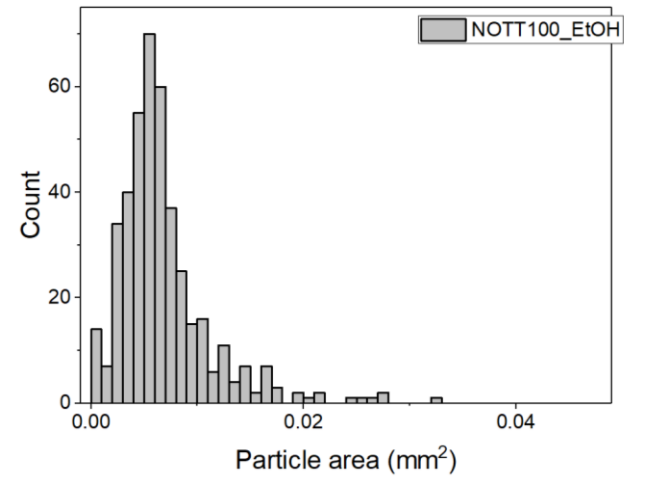

Figure 37: An example of a histogram of particle size distribution of the NOTT-100 crystallites. Using the resulting histogram, a scatter graph of particle count and bin centre was plotted.

Fifty bins were chosen as this represented a relatively even size distribution of particles for the total number of particles in the images.

Then the number of counts for each bin was plotted against the bin centres to make a scatter graph (Figure 38).

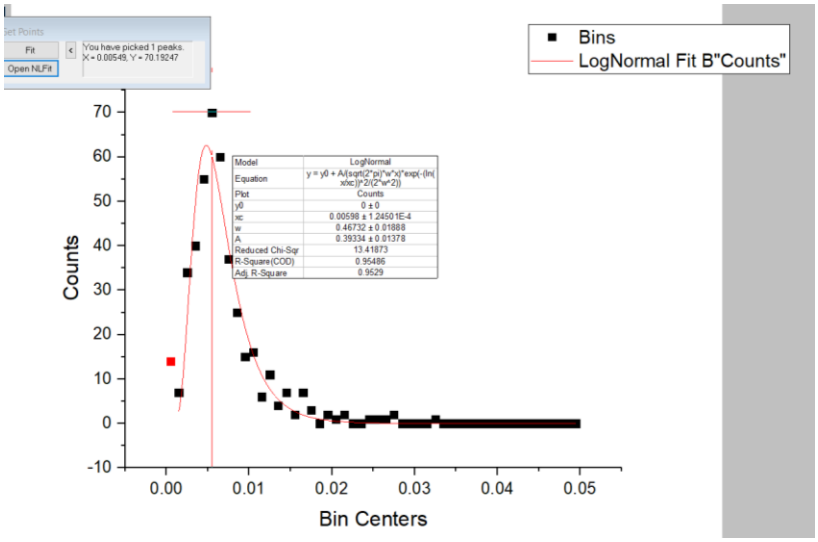

Figure 38: An example plot of the bin centres from the particle size distribution histogram against the particle count for these bins. The lognormal fit is shown in red.

The resulting plot was fitted using a lognormal function and y0 was set to 0, as at y=0 there should be no particles present. For SEM images the first bin was masked when fitting the lognormal function, this was due to the fact that the first bin was often very large and was not representative of the actual crystal size as it included image 'speckle' that was not satisfactorily removed by deleting the 3 x 3 pixel objects. The first bin was not masked for optical images as being significantly larger the first bin was representative of the actual crystal size. Finally, the histogram and lognormal curve were overlaid.

4. References

1 S. James, *Compr. Inorg. Chem. II (Second Ed. From Elem. to Appl.*, 2013, **5**, 45–71.

2 H.-C. '"Joe"' Zhou and S. Kitagawa, *J. Solid State Chem.*, 2015, **223**, 1.

3 P. Z. Moghadam, A. Li, S. B. Wiggin, A. Tao, A. G. P. Maloney, P. A. Wood, S. C. Ward and D. Fairen-Jimenez, *Chem. Mater.*, 2017, **29**, 2618–2625.

4 H. Furukawa, N. Ko, Y. B. Go, N. Aratani, S. B. Choi, E. Choi, A. O. Yazaydin, R. Q. Snurr, M. O'Keeffe, J. Kim and O. M. Yaghi, *Science*, 2010, **329**, 424–8.

5 K. S. Walton and R. Q. Snurr, *J. Am. Chem. Soc.*, 2007, **129**, 8552–8556.

6 J. Čejka, *Angew. Chemie Int. Ed.*, 2012, **51**, 4782–4783.

7 F. Gándara, H. Furukawa, S. Lee and O. M. Yaghi, *J. Am. Chem. Soc.*, 2014, **136**, 5271–5274.

8 J. Sculley, D. Yuan and H.-C. Zhou, *Energy Environ. Sci.*, 2011, **4**, 2721.

9 D. Alezi, Y. Belmabkhout, M. Suyetin, P. M. Bhatt, L. J. Weseliński, V. Solovyeva, K. Adil, I. Spanopoulos, P. N. Trikalitis, A. H. Emwas and M. Eddaoudi, *J. Am. Chem. Soc.*, 2015, **137**, 13308–13318.

10 J.-R. Li, J. Sculley and H.-C. Zhou, *Chem. Rev.*, 2012, **112**, 869–932.

11 H. Bux, C. Chmelik, R. Krishna and J. Caro, *J. Memb. Sci.*, 2011, **369**, 284–289.

12 M. Kang, D. W. Kang and C. S. Hong, *Dalt. Trans.*, 2019, **48**, 2263–2270.

13 C. Orellana-Tavra, E. F. Baxter, T. Tian, T. D. Bennett, N. K. H. Slater, A. K. Cheetham and D. Fairen-Jimenez, *Chem. Commun.*, 2015, **51**, 13878–13881.

14 M.-X. Wu and Y.-W. Yang, *Adv. Mater.*, 2017, **29**, 1606134.

15 N. L. Torad, Y. Li, S. Ishihara, K. Ariga, Y. Kamachi, H.-Y. Lian, H. Hamoudi, Y. Sakka, W. Chaikittisilp, K. C.-W. Wu and Y. Yamauchi, *Chem. Lett.*, 2014, **43**, 717–719.

16 J. Della Rocca, D. Liu and W. Lin, *Acc. Chem. Res.*, 2011, **3**, 957–968.

17 S. Keskin and S. Kızılel, *Ind. Eng. Chem. Res*, 2011, **50**, 1799–1812.

18 S. Wuttke, A. Zimpel, T. Bein, S. Braig, K. Stoiber, A. Vollmar, D. Müller, K. Haastert-Talini, J. Schaeske, M. Stiesch, G. Zahn, A. Mohmeyer, P. Behrens, O. Eickelberg, D. A. Bölükbas and S. Meiners, *Adv. Healthc. Mater.*, 2017, **6**, 1600818.

19 X. Cai, X. Deng, Z. Xie, Y. Shi, M. Pang and J. Lin, *Chem. Eng. J.*, 2019, **358**,

369–378.

20 Y. Lü, W. Zhan, Y. He, Y. Wang, X. Kong, Q. Kuang, Z. Xie and L. Zheng, *ACS Appl. Mater. Interfaces*, 2014, **6**, 4186–4195.

21 M. R. Tchalala, P. M. Bhatt, K. N. Chappanda, S. R. Tavares, K. Adil, Y. Belmabkhout, A. Shkurenko, A. Cadiau, N. Heymans, G. De Weireld, G. Maurin, K. N. Salama and M. Eddaoudi, *Nat. Commun.*, 2019, **10**, 1328.

22 X. Zhu, H. Zheng, X. Wei, Z. Lin, L. Guo, B. Qiu and G. Chen, *Chem. Commun.*, 2013, **49**, 1276.

23 Y. Cui, R. Song, J. Yu, M. Liu, Z. Wang, C. Wu, Y. Yang, Z. Wang, B. Chen and G. Qian, *Adv. Mater.*, 2015, **27**, 1420–1425.

24 S. Rojas-Buzo, P. García and A. Corma, *Catal. Sci. Technol*, 2019, **9**, 146.

25 F. X. Llabrés i Xamena, A. Abad, A. Corma and H. Garcia, *J. Catal.*, 2007, **250**, 294–298.

26 P. García-García, M. Müller and A. Corma, *Chem. Sci.*, 2014, **5**, 2979–3007.

27 J. Lee, O. K. Farha, J. Roberts, K. A. Scheidt, S. T. Nguyen and J. T. Hupp, *Chem. Soc. Rev.*, 2009, **38**, 1450–1459.

28 S. T. Meek, J. A. Greathouse and M. D. Allendorf, *Adv. Mater.*, 2011, **23**, 249–267.

29 A. J. Howarth, A. W. Peters, N. A. Vermeulen, T. C. Wang, J. T. Hupp and O. K. Farha, *Chem. Mater.*, 2017, 29, 26–39.

30 R. J. Marshall, C. L. Hobday, C. F. Murphie, S. L. Griffin, C. A. Morrison, S. A. Moggach and R. S. Forgan, *J. Mater. Chem. A*, 2016, **4**, 6955–6963.

31 B. Y. Li, H. Bux, A. Feldhoff, G. Li, W. Yang and J. Caro, 2010, 3322–3326.

32 S. Tanaka, K. Fujita, Y. Miyake, M. Miyamoto, Y. Hasegawa, T. Makino, S. Van der Perre, J. Cousin Saint Remi, T. Van Assche, G. V. Baron and J. F. M. Denayer, *J. Phys. Chem. C*, 2015, **119**, 28430–28439.

33 L. H. Wee, M. R. Lohe, N. Janssens, S. Kaskel and J. A. Martens, *J. Mater. Chem.*, 2012, **22**, 13742–13746.

34 X. Lan, N. Huang, J. Wang and T. Wang, *Chem. Commun.*, 2018, **54**, 584–587.

35 N. T. S. Phan, K. K. A. Le and T. D. Phan, *Appl. Catal. A Gen.*, 2010, **382**, 246–253.

36 E. V. Perez, C. Karunaweera, I. H. Musselman, K. J. Balkus and J. P. Ferraris, *Processes*, 2016, 4.

37 H. Cho, D. Yang, J. Kim, S. Jeong and W. Ahn, *Catal. Today*, 2012, **185**, 35–40.

38 S. Chen, M. Xue, Y. Li, Y. Pan, L. Zhu and S. Qiu, *J. Mater. Chem. A*, 2015, **3**, 20145–20152.

39 W. Li, Y. Zhang, Z. Xu, Q. Meng, Z. Fan, S. Ye and G. Zhang, *Angew. Chemie Int. Ed.*, 2016, **55**, 955–959.

40 S. M. Moosavi, A. Chidambaram, L. Talirz, M. Haranczyk, K. C. Stylianou and B. Smit, *Nat. Commun.*, 2019, **10**, 539.

41 K.-Y. Andrew Lin and Y.-T. Hsieh, *J. Taiwan Inst. Chem. Eng.*, 2015, **50**, 223–228.

42 Searching on Google scholar for 'metal-organic framework OR MOF AND SEM', https://scholar.google.co.uk/scholar?hl=en&as_sdt=0%2C5&q=metal-organic+framework+OR+MOF+AND+SEM&btnG=&oq=metal, (accessed 25 July 2019).

43 C. Wiktor, S. Turner, D. Zacher, R. A. Fischer and G. Van Tendeloo, *Microporous Mesoporous Mater.*, 2012, **162**, 131–135.

44 S. Turner, O. I. Lebedev, F. Schröder, D. Esken, R. A. Fischer and G. Van Tendeloo, , DOI:10.1021/cm801165s.

45 M. Kaszuba, D. McKnight, M. T. Connah, F. K. McNeil-Watson and U. Nobbmann, *J. Nanoparticle Res.*, 2008, **10**, 823–829.

46 K. K. Tanabe, C. A. Allen and S. M. Cohen, *Angew. Chemie Int. Ed.*, 2010, **49**, 9730–9733.

47 J. Park, D. Yuan, K. T. Pham, J.-R. Li, A. Yakovenko and H.-C. Zhou, *J. Am. Chem. Soc.*, 2012, **134**, 99–102.

48 M. Eddaoudi, J. Kim, N. Rosi, D. Vodak and O. M. Yaghi, *Science (80-.).*, 2002, **295**, 469–472.

49 S. Castellanos, F. Kapteijn and J. Gascon, *CrystEngComm*, 2016, 18, 4006–4012.

50 J. M. Cole, *Acta Crystallogr. Sect. A Found. Crystallogr.*, 2008, 64, 259–271.

51 Y. Hirshberg, *J. Am. Chem. Soc.*, 1956, **78**, 2304–2312.

52 S. Prager, I. Burghardt and A. Dreuw, *J. Phys. Chem. A*, 2014, **118**, 1339–1349.

53 V. Pimienta, D. Lavabre, G. Levy, A. Samat, R. Guglielmetti and J. C. Micheau, *Kinetic Analysis of Photochromic Systems under Continuous*

Irradiation. Application to Spiropyrans, 1996.

54 P. B. Markworth, B. D. Adamson, N. J. A. Coughlan, L. Goerigk and E. J. Bieske, *Phys. Chem. Chem. Phys*, **17**, 25676.

55 T. Stafforst and D. Hilvert, , DOI:10.1039/b818050d.

56 N. Shao, Y. Zhang, S. Cheung, R. Yang, W. Chan, T. Mo, K. Li and F. Liu, *Anal. Chem.*, 2005, **77**, 7294–303.

57 K. Healey, W. Liang, P. D. Southon, T. L. Church and D. M. D'Alessandro, *J. Mater. Chem. A*, 2016, **4**, 10816–10819.

58 H. A. Schwartz, S. Olthof, D. Schaniel, K. Meerholz and U. Ruschewitz, *Inorg. Chem.*, 2017, **56**, 13100–13110.

59 R. Rosario, D. Gust, M. Hayes, F. Jahnke, J. Springer and A. A. Garcia, *Langmuir*, 2002, **18**, 8062–8069.

60 D. E. Williams, C. R. Martin, E. A. Dolgopolova, A. Swifton, D. C. Godfrey, O. A. Ejegbavwo, P. J. Pellechia, M. D. Smith and N. B. Shustova, *J. Am. Chem. Soc.*, 2018, **140**, 7611–7622.

61 K. Healey, W. Liang, P. D. Southon, T. L. Church and D. M. D'Alessandro, *J. Mater. Chem. A*, 2016, **4**, 10816–10819.

62 J. Xu, J. Liu, Z. Li, X. Wang, Y. Xu, S. Chen and Z. Wang, *New J. Chem.*, 2019, **43**, 4092–4099.

63 Water scarcity, https://www.worldwildlife.org/threats/water-scarcity, (accessed 30 April 2019).

64 H. T. El-Dessouky and H. M. Ettouney, *Fundamentals of salt water desalination*, Elsevier, 2002.

65 V. G. Gude, *Water Res.*, 2016, **89**, 87–106.

66 M. Elimelech and W. A. Phillip, *Science (80-.).*, 2011, 333, 712–717.

67 K. Al-Shayji and E. Aleisa, *Energy*, 2018, **158**, 681–692.

68 X. Liu, N. K. Demir, Z. Wu and K. Li, *J. Am. Chem. Soc*, 2015, **137**, 58.

69 Y. Sun and H. C. Zhou, *Sci. Technol. Adv. Mater.*, 2015, 16.

70 C. A. Trickett, K. J. Gagnon, S. Lee, F. Gándara, H. B. Bürgi and O. M. Yaghi, *Angew. Chemie - Int. Ed.*, 2015, **54**, 11162–11167.

71 X. Wang, L. Zhai, Y. Wang, R. Li, X. Gu, Y. Di Yuan, Y. Qian, Z. Hu and D. Zhao, *ACS Appl. Mater. Interfaces*, 2017, **9**, 37848–37855.

72 X. Liu, N. K. Demir, Z. Wu and K. Li, *J. Am. Chem. Soc.*, 2015, **137**, 6999–7002.

73 R. C. Bertelson, in *Organic Photochromic and Thermochromic Compounds*, Kluwer Academic Publishers, Boston, 2002, pp. 11–83.
74 S. Bao, X. Cai, Y. Shi and M. Pang, 2017, **19**, 1875.
75 B. Bueken, H. Reinsch, N. Reimer, I. Stassen, F. Vermoortele, R. Ameloot, N. Stock, C. E. A. Kirschhock and D. De Vos, *Chem. Commun*, 2014, **50**, 10055.
76 O. V. Gutov, W. Bury, D. A. Gomez-Gualdron, V. Krungleviciute, D. Fairen-Jimenez, J. E. Mondloch, A. A. Sarjeant, S. S. Al-Juaid, R. Q. Snurr, J. T. Hupp, T. Yildirim and O. K. Farha, *Chem. - A Eur. J.*, 2014, **20**, 12389–12393.
77 O. V. Gutov, S. Molina, E. C. Escudero-Adán and A. Shafir, *Chem. - A Eur. J.*, 2016, **22**, 13582–13587.
78 T. D. Bennett and A. K. Cheetham, *Acc. Chem. Res*, 2014, **47**, 35.
79 T. D. Bennett, A. L. Goodwin, M. T. Dove, D. A. Keen, M. G. Tucker, E. R. Barney, A. K. Soper, E. G. Bithell, J. C. Tan and A. K. Cheetham, *Phys. Rev. Lett.*, 2010, **104**, 115503.
80 C. Orellana-Tavra, E. F. Baxter, T. Tian, T. D. Bennett, N. K. H. Slater, A. K. Cheetham and D. Fairen-Jimenez, *Chem. Commun.*, 2015, **51**, 13878–13881.
81 Pair Distribution Function | Diamond Light Source - Diamond Synchrotron Facilities for Industry - Diamond Light Source, https://www.diamond.ac.uk/industry/Techniques-Available/X-ray-Pair-Distribution-Function-PDF.html, (accessed 9 May 2019).
82 J. Duan, Y. Pan, G. Liu and W. Jin, *Curr. Opin. Chem. Eng.*, 2018, 20, 122–131.
83 X. Lin, I. Telepeni, A. J. Blake, A. Dailly, C. M. Brown, J. M. Simmons, M. Zoppi, G. S. Walker, K. M. Thomas, T. J. Mays, P. Hubberstey, N. R. Champness and M. Schröder, *J. Am. Chem. Soc.*, 2009, **131**, 2159–2171.
84 K. Ren, X.-F. Guo, Y. Tang, B. hui Huang and H. Wang, *Analyst*, , DOI:10.1039/d0an01566k.
85 V. Stavila, C. Schneider, C. Mowry, T. R. Zeitler, J. A. Greathouse, A. L. Robinson, J. M. Denning, J. Volponi, K. Leong, W. Quan, M. Tu, R. A. Fischer and M. D. Allendorf, *Adv. Funct. Mater.*, 2016, **26**, 1699–1707.
86 M. Sandström, I. Persson, P. Persson, E. K. Euranto, T. Brekke, D. W. Aksnes and T. Tokii, *Acta Chem. Scand.*, 1990, **44**, 653–675.
87 V. Gutmann, *Electrochim. Acta*, 1976, **21**, 661–670.
88 C. Reichardt, in *Solvents and Solvent Effects in Organic Chemistry*, Wiley-

VCH Verlag GmbH & Co. KGaA, Weinheim, FRG, 2004, pp. 389–469.

89 I. Smallwood, *Handbook of Organic Solvent Properties*, Arnold, 1996.

90 M. Kadhom and B. Deng, *Appl. Mater. Today*, 2018, 11, 219–230.

91 M. Dahanayaka, R. Babicheva, Z. Chen, A. W. K. Law, M. S. Wu and K. Zhou, *Appl. Surf. Sci.*, , DOI:10.1016/j.apsusc.2019.144198.

92 C. P. Krap, R. Newby, A. Dhakshinamoorthy, H. García, I. Cebula, T. L. Easun, M. Savage, J. E. Eyley, S. Gao, A. J. Blake, W. Lewis, P. H. Beton, M. R. Warren, D. R. Allan, M. D. Frogley, C. C. Tang, G. Cinque, S. Yang and M. Schröder, *Inorg. Chem.*, 2016, **55**, 1076–1088.

93 M. Chong, PhD Thesis, The University of Nottingham, 2016.

94 A. Nevin, PhD Thesis, The University of Nottingham, 2016.

95 ImageJ Adjutable Watershed, http://imagejdocu.tudor.lu/doku.php?id=plugin:segmentation:adjustable_watershed:start, (accessed 3 November 2020).

5. Appendix

Appendix 1 – General catalytic cycle of the Suzuki-Miyaura reaction:

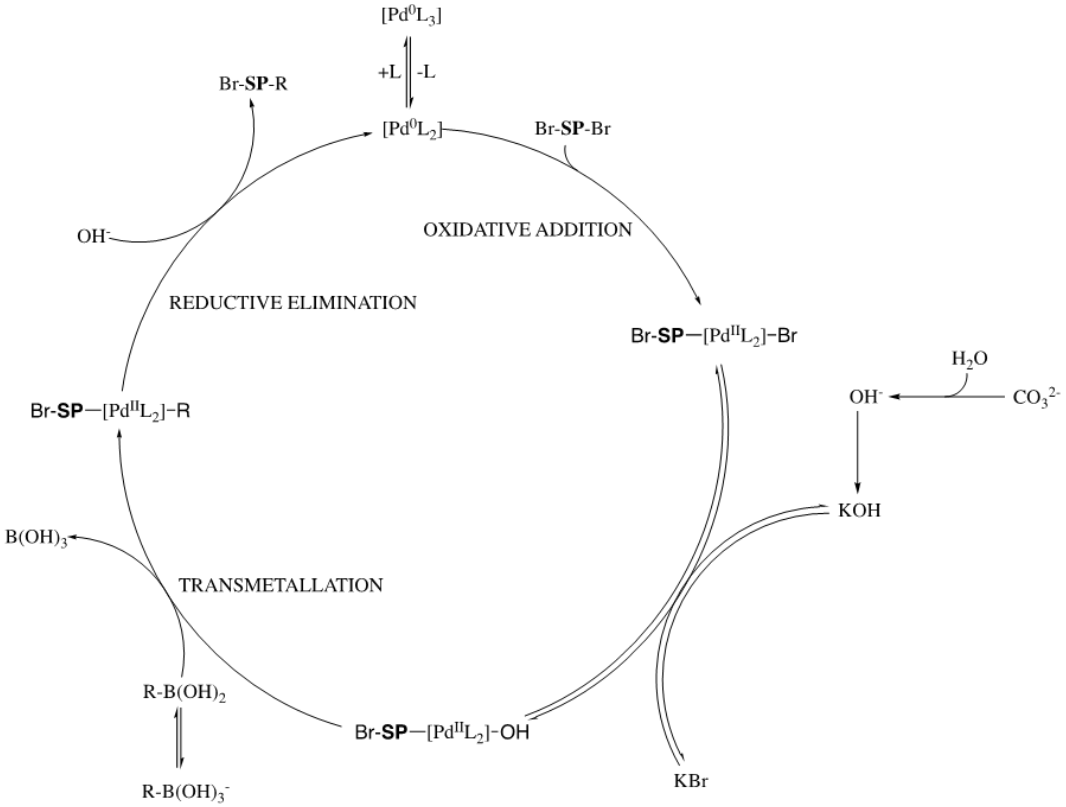

Appendix 2 – Combinatorial synthesis

Combinatorial 1

L1	Metal salt	Solvent	Modulator	Temperature	Time
10 mg	$ZrCl_4$ 25 mg	1 ml DMF	0.01 ml 1M HCl	60 °C	3 days
10 mg	$ZrCl_4$ 25 mg	1 ml DMF	0.05 ml 1M HCl	60 °C	3 days
10 mg	$ZrCl_4$ 25 mg	1 ml DMF	0.3 ml 1M HCl	60 °C	3 days
10 mg	$ZrCl_4$ 25 mg	1 ml DMF	0.4 ml 1M HCl	60 °C	3 days
10 mg	$ZrCl_4$ 25 mg	1 ml DMF	0.5 ml 1M HCl	60 °C	3 days
10 mg	$ZrCl_4$ 25 mg	1 ml DMF	1 drop of conc. HCl	60 °C	3 days
10 mg	$ZrCl_4$ 25 mg	1 ml DMF	2 drop of conc. HCl	60 °C	3 days
10 mg	$ZrCl_4$ 25 mg	1 ml DMF	3 drop of conc. HCl	60 °C	3 days
10 mg	$ZrCl_4$ 25 mg	1 ml DMF	4 drop of conc. HCl	60 °C	3 days
10 mg	$ZrCl_4$ 25 mg	1 ml DMF	4 drop of conc. HNO_3	40 °C	3 days
10 mg	$ZrCl_4$ 25 mg	1 ml DMF	5 drop of conc. HNO_3	40 °C	3 days
10 mg	$ZrCl_4$ 25 mg	1 ml DMF	6 drop of conc. HNO_3	40 °C	3 days
10 mg	$ZrCl_4$ 25 mg	1 ml DMF	5 drop of conc. HNO_3	40 °C	3 days
10 mg	$ZrCl_4$ 25 mg	1 ml DMF	0.2 ml 1M HCl	40 °C	3 days
10 mg	$ZrCl_4$ 25 mg	1 ml DMF	4 drop of conc. HNO_3	60 °C	3 days
10 mg	$ZrCl_4$ 25 mg	1 ml DMF	5 drop of conc. HNO_3	60 °C	3 days
10 mg	$ZrCl_4$ 25 mg	1 ml DMF	6 drop of conc. HNO_3	60 °C	3 days

Combinatorial 2

L1	Metal salt	Solvent	Modulator	Temperature	Time
10 mg	$ZrCl_4$ 25 mg	1 ml DMF	5 drop of conc. HNO_3	60 °C	3 days
-	$ZrCl_4$ 25 mg	1 ml DMF	5 drop of conc. HNO_3	60 °C	3 days
10 mg	-	1 ml DMF	5 drop of conc. HNO_3	60 °C	3 days
10 mg	$ZrCl_4$ 25 mg	1 ml DMF	0.004 ml conc. HCl and 0.026g of proline	60 °C	3 days

Combinatorial 3

L1	Metal salt	Solvent	Modulator	Temperature	Time
10 mg	$ZrCl_4$ 25 mg	1 ml DMF	5 drop of conc. HNO_3	70 °C	3 days
-	$ZrCl_4$ 25 mg	1 ml DMF	5 drop of conc. HNO_3	70 °C	3 days
10 mg	-	1 ml DMF	5 drop of conc. HNO_3	70 °C	3 days

Combinatorial 4

L1	Metal salt	Solvent	Modulator	Temperature	Time
10 mg	$ZrCl_4$ 25 mg	1 ml DMF	0.01 ml 1M HCl	60 °C	3 days
10 mg	$ZrCl_4$ 25 mg	1 ml DMF	0.02 ml 1M HCl	60 °C	3 days
10 mg	$ZrCl_4$ 25 mg	1 ml DMF	0.03 ml 1M HCl	60 °C	3 days
10 mg	$ZrCl_4$ 25 mg	1 ml DMF	0.04 ml 1M HCl	60 °C	3 days
10 mg	$ZrCl_4$ 25 mg	1 ml DMF	5 drop of conc. HCl	60 °C	3 days
10 mg	$ZrCl_4$ 25 mg	1 ml DMF	6 drop of conc. HCl	60 °C	3 days
10 mg	$ZrCl_4$ 25 mg	1 ml DMF	100 mg 4-amino benzoic acid	60 °C	3 days
10 mg	$ZrCl_4$ 25 mg	1 ml DMF	500 mg 4-amino benzoic acid	60 °C	3 days
10 mg	$ZrCl_4$ 25 mg	1 ml DMF	0.1 ml formic acid	60 °C	3 days
10 mg	$ZrCl_4$ 25 mg	1 ml DMF	0.5 ml formic acid	60 °C	3 days
10 mg	$ZrCl_4$ 25 mg	1 ml DMF	1 ml formic acid	60 °C	3 days
10 mg	$ZrCl_4$ 25 mg	1 ml DMF	1.5 ml formic acid	60 °C	3 days
10 mg	$ZrCl_4$ 25 mg	1 ml DMF	0.008 ml conc. HCl and 0.026g of proline	60 °C	3 days
10 mg	$ZrCl_4$ 25 mg	1 ml DMF	0.004 ml conc. HCl and 0.052g of proline	60 °C	3 days
10 mg	$ZrCl_4$ 25 mg	1 ml DMF	0.01 ml trifluoroacetic acid	60 °C	3 days
10 mg	$ZrCl_4$ 25 mg	1 ml DMF	0.1 ml trifluoroacetic acid	60 °C	3 days
10 mg	$ZrCl_4$ 25 mg	1 ml DMF	1 ml trifluoroacetic acid	60 °C	3 days
10 mg	$ZrCl_4$ 25 mg	1 ml DMF	6 drop of conc. HNO_3	60 °C	3 days

Combinatorial 5

L1	Metal salt	Solvent	Modulator	Temperature	Time
10 mg	$ZrCl_4$ 25 mg	1 ml DMF	0.01 ml 1M HCl	50 °C	3 days
10 mg	$ZrCl_4$ 25 mg	1 ml DMF	2 drop of conc. HCl	50 °C	3 days
10 mg	$ZrCl_4$ 25 mg	1 ml DMF	3 drop of conc. HCl	50 °C	3 days
10 mg	$ZrCl_4$ 25 mg	1 ml DMF	4 drop of conc. HCl	50 °C	3 days
10 mg	$ZrCl_4$ 25 mg	1 ml DMF	5 drop of conc. HNO_3	50 °C	3 days
10 mg	$ZrCl_4$ 25 mg	1 ml DMF	0.004 ml conc. HCl and 0.052g of proline	50 °C	3 days

Combinatorial 6

L2	Metal salt	Solvent	Modulator	Temperature	Time
10 mg	$ZrCl_4$ 25 mg	1 ml DMF	0.01 ml 1M HCl	60 °C	3 days
10 mg	$ZrCl_4$ 25 mg	1 ml DMF	2 drop of conc. HCl	60 °C	3 days
10 mg	$ZrCl_4$ 25 mg	1 ml DMF	3 drop of conc. HCl	60 °C	3 days
10 mg	$ZrCl_4$ 25 mg	1 ml DMF	4 drop of conc. HCl	60 °C	3 days
10 mg	$ZrCl_4$ 25 mg	1 ml DMF	5 drop of conc. HNO_3	60 °C	3 days
10 mg	$ZrCl_4$ 25 mg	1 ml DMF	0.004 ml conc. HCl and 0.052g of proline	60 °C	3 days

Combinatorial 7

L1	Metal salt	Solvent	Modulator	Temperature	Time
10 mg	$ZrCl_4$ 25 mg	1 ml DMF	0.01 ml 1M HCl	60 °C	3 days
10 mg	$ZrCl_4$ 25 mg	1 ml DMF	0.02 ml 1M HCl	60 °C	3 days
10 mg	$ZrCl_4$ 25 mg	1 ml DMF	0.03 ml 1M HCl	60 °C	3 days
10 mg	$ZrCl_4$ 25 mg	1 ml DMF	0.04 ml 1M HCl	60 °C	3 days
10 mg	$ZrCl_4$ 25 mg	1 ml DMF	no modulator	60 °C	3 days
L2	**Metal salt**	**Solvent**	**Modulator**	**Temperature**	**Time**
10 mg	$ZrCl_4$ 25 mg	1 ml DMF	0.01 ml 1M HCl	60 °C	3 days
10 mg	$ZrCl_4$ 25 mg	1 ml DMF	0.02 ml 1M HCl	60 °C	3 days
10 mg	$ZrCl_4$ 25 mg	1 ml DMF	0.03 ml 1M HCl	60 °C	3 days
10 mg	$ZrCl_4$ 25 mg	1 ml DMF	0.04 ml 1M HCl	60 °C	3 days
10 mg	$ZrCl_4$ 25 mg	1 ml DMF	no modulator	60 °C	3 days
Control experiments	**Metal salt**	**Solvent**	**Modulator**	**Temperature**	**Time**
-	$ZrCl_4$ 25 mg	1 ml DMF	0.01 ml 1M HCl	60 °C	3 days
-	$ZrCl_4$ 25 mg	1 ml DMF	0.02 ml 1M HCl	60 °C	3 days
-	$ZrCl_4$ 25 mg	1 ml DMF	0.03 ml 1M HCl	60 °C	3 days
-	$ZrCl_4$ 25 mg	1 ml DMF	0.04 ml 1M HCl	60 °C	3 days
-	$ZrCl_4$ 25 mg	1 ml DMF	no modulator	60 °C	3 days

Combinatorial 8

L1	Metal salt	Solvent	Modulator	Temperature	Time
10 mg	$ZrCl_4$ 25 mg	1 ml DEF	0.075 ml conc. HCl	50 °C	10 days
10 mg	$ZrCl_4$ 25 mg	1 ml DEF	0.08 ml conc. HCl	50 °C	10 days
10 mg	$ZrCl_4$ 25 mg	1 ml DEF	0.085 ml conc. HCl	50 °C	10 days
10 mg	$ZrCl_4$ 25 mg	1 ml DEF	0.09 ml conc. HCl	50 °C	10 days
10 mg	$ZrCl_4$ 25 mg	1 ml DEF	0.095 ml conc. HCl	50 °C	10 days
10 mg	$ZrCl_4$ 25 mg	1 ml DEF	0.075 ml conc. HCl	40 °C	10 days
10 mg	$ZrCl_4$ 25 mg	1 ml DEF	0.08 ml conc. HCl	40 °C	10 days
10 mg	$ZrCl_4$ 25 mg	1 ml DEF	0.085 ml conc. HCl	40 °C	10 days
10 mg	$ZrCl_4$ 25 mg	1 ml DEF	0.09 ml conc. HCl	40 °C	10 days
10 mg	$ZrCl_4$ 25 mg	1 ml DEF	0.095 ml conc. HCl	40 °C	10 days

Combinatorial 9

L1	Metal salt	Solvent	Modulator	Temperature	Time
10 mg	$AlN_3O_9.9H_2O$ 41 mg	1 ml DMF	no modulator	60 °C	15 days
10 mg	$AlN_3O_9.9H_2O$ 80 mg	1 ml DMF	no modulator	60 °C	15 days
10 mg	$AlN_3O_9.9H_2O$ 122 mg	1 ml DMF	no modulator	60 °C	15 days
10 mg	$AlN_3O_9.9H_2O$ 20 mg	1 ml DMF	no modulator	60 °C	15 days
10 mg	$AlN_3O_9.9H_2O$ 14 mg	1 ml DMF	no modulator	60 °C	15 days
10 mg	$Ga(NO_3)_3 \cdot xH_2O$ 28 mg	1 ml DMF	no modulator	60 °C	15 days
10 mg	$Ga(NO_3)_3 \cdot xH_2O$ 55 mg	1 ml DMF	no modulator	60 °C	15 days
10 mg	$Ga(NO_3)_3 \cdot xH_2O$ 83 mg	1 ml DMF	no modulator	60 °C	15 days
10 mg	$Ga(NO_3)_3 \cdot xH_2O$ 14 mg	1 ml DMF	no modulator	60 °C	15 days
10 mg	$Ga(NO_3)_3 \cdot xH_2O$ 9 mg	1 ml DMF	no modulator	60 °C	15 days
10 mg	$GdH_{12}N_3O_{15}$ 49 mg	1 ml DMF	no modulator	60 °C	15 days
10 mg	$GdH_{12}N_3O_{15}$ 97 mg	1 ml DMF	no modulator	60 °C	15 days
10 mg	$GdH_{12}N_3O_{15}$ 146 mg	1 ml DMF	no modulator	60 °C	15 days
10 mg	$GdH_{12}N_3O_{15}$ 24 mg	1 ml DMF	no modulator	60 °C	15 days
10 mg	$GdH_{12}N_3O_{15}$ 16 mg	1 ml DMF	no modulator	60 °C	15 days

Combinatorial 10

L1	Metal salt	Solvent	Modulator	Temperature	Time
10 mg	$Ga(NO_3)_3 \cdot xH_2O$ 9 mg	1 ml DMF	0.01 ml 1M HCl	60 °C	15 days
10 mg	$Ga(NO_3)_3 \cdot xH_2O$ 9 mg	1 ml DMF	0.05 ml 1M HCl	60 °C	15 days
10 mg	$Ga(NO_3)_3 \cdot xH_2O$ 9 mg	1 ml DMF	0.02 ml conc. HNO_3	60 °C	15 days
10 mg	$Ga(NO_3)_3 \cdot xH_2O$ 9 mg	1 ml DMF	0.035 ml conc. HNO_3	60 °C	15 days
10 mg	$GdH_{12}N_3O_{15}$ 16 mg	1 ml DMF	0.01 ml 1M HCl	60 °C	15 days
10 mg	$GdH_{12}N_3O_{15}$ 16 mg	1 ml DMF	0.05 ml 1M HCl	60 °C	15 days
10 mg	$GdH_{12}N_3O_{15}$ 16 mg	1 ml DMF	0.02 ml conc. HNO_3	60 °C	15 days
10 mg	$GdH_{12}N_3O_{15}$ 16 mg	1 ml DMF	0.035 ml conc. HNO_3	60 °C	15 days
10 mg	$Ga(NO_3)_3 \cdot xH_2O$ 9 mg	1 ml DMF	0.05 ml conc. HNO_3	60 °C	15 days
10 mg	$Ga(NO_3)_3 \cdot xH_2O$ 9 mg	1 ml DMF	0.075 ml conc. HNO_3	60 °C	15 days
10 mg	$GdH_{12}N_3O_{15}$ 16 mg	1 ml DMF	0.075 ml 1M HCl	60 °C	15 days
10 mg	$GdH_{12}N_3O_{15}$ 16 mg	1 ml DMF	0.1 ml 1M HCl	60 °C	15 days

Appendix 3 - The PXRD pattern for $ZrCl_4$.

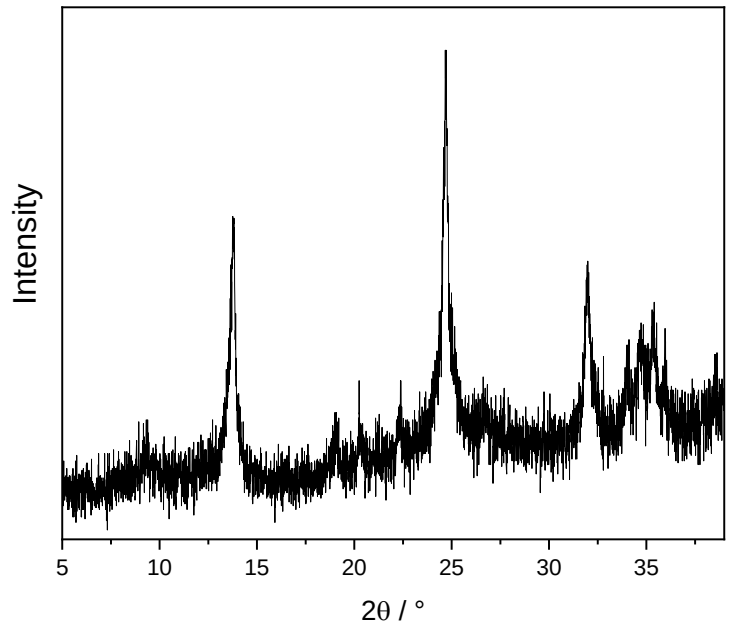

Appendix 4 - Plots of the particle size distribution histograms curve centre (x_c) for the secondary exchange solvents and width (w) against the different solvent parameters that had no correlation with a linear fit (red line) and accompanying R^2 values.

w | **x_c**

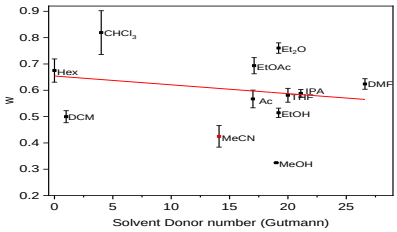

R^2 = 0.05

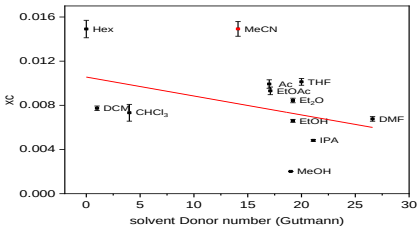

R^2 = 0.22

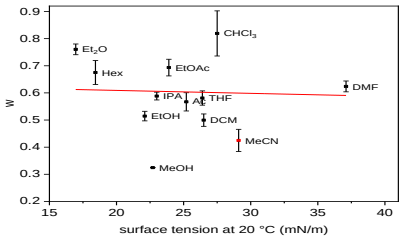

R^2 = 0.00

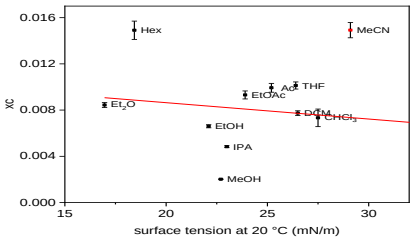

R^2 = 0.05

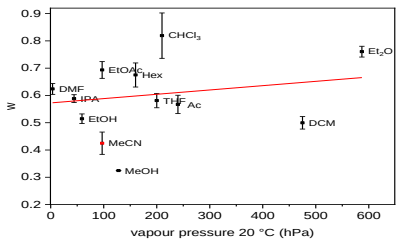

R^2 = 0.04

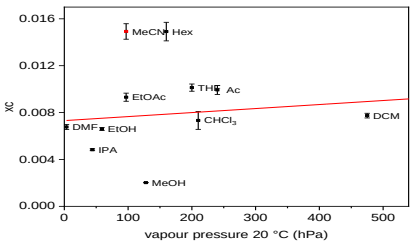

R^2 = 0.04

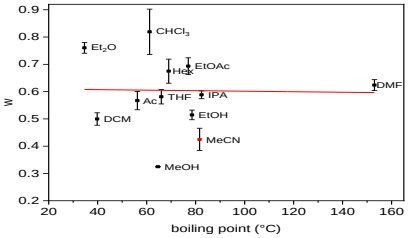

R^2 = 0.00

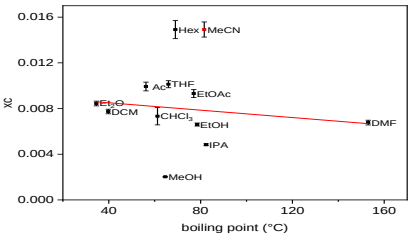

R^2 = 0.02